

The Sloan Digital Sky Survey Reverberation Mapping Project: Systematic Investigations of Short-timescale CIV Broad Absorption Line Variability

Z. S. Hemler¹, C. J. Grier^{1,2}, W. N. Brandt^{1,2,3}, P. B. Hall⁴, Keith Horne⁵, Yue Shen^{6,7,11}, J. R. Trump⁸, D. P. Schneider^{1,2}, M. Vivek^{1,2}, Dmitry Bizyaev^{9,10}, Audrey Oravetz⁹, Daniel Oravetz⁹, and Kaike Pan⁹, Department of Astronomy and Astrophysics, Eberly College of Science, The Pennsylvania State University, 525 Davey Laboratory, University Park, PA 16802, USA

Institute for Gravitation & the Cosmos, The Pennsylvania State University, University Park, PA 16802, USA

Department of Physics, The Pennsylvania State University, University Park, PA 16802, USA

Department of Physics and Astronomy, York University, Toronto, ON M3J 1P3, Canada

Supa Physics and Astronomy, University of St. Andrews, Fife, KY16 9SS, Scotland, UK

Department of Astronomy, University of Illinois at Urbana-Champaign, Urbana, IL 61801, USA

National Center for Supercomputing Applications, University of Illinois at Urbana-Champaign, Urbana, IL 61801, USA

Popartment of Physics, University of Connecticut, 2152 Hillside Road, Unit 3046, Storrs, CT 06269, USA

Apache Point Observatory and New Mexico State University, P.O. Box 59, sunspot, NM, 88349-0059, USA

Sternberg Astronomical Institute, Moscow State University, Moscow, Russia

Received 2018 July 28; revised 2018 October 24; accepted 2018 October 27; published 2019 February 6

Abstract

We systematically investigate short-timescale (<10 day rest-frame) C IV broad absorption-line (BAL) variability to constrain quasar-wind properties and provide insights into BAL-variability mechanisms in quasars. We employ data taken by the Sloan Digital Sky Survey Reverberation Mapping project, as the rapid cadence of these observations provides a novel opportunity to probe BAL variability on shorter rest-frame timescales than have previously been explored. In a sample of 27 quasars with a median of 58 spectral epochs per quasar, we have identified 15 quasars (55 $^{+18}_{-14}\%$), 19 of 37 C IV BAL troughs (51 $^{+15}_{-12}\%$), and 54 of 1460 epoch pairs (3.7% \pm 0.5%) that exhibit significant C IV BAL equivalent-width variability on timescales of less than 10 days in the quasar rest frame. These frequencies indicate that such variability is common among quasars and BALs, though somewhat rare among epoch pairs. Thus, models describing BALs and their behavior must account for variability on timescales down to less than a day in the quasar rest frame. We also examine a variety of spectral characteristics and find that, in some cases, BAL variability is best described by ionization-state changes, while other cases are more consistent with changes in covering fraction or column density. We adopt a simple model to constrain the density and radial distance of two outflows appearing to vary by ionization-state changes, yielding outflow density lower limits consistent with previous work.

Key words: galaxies: active – galaxies: kinematics and dynamics – galaxies: nuclei – quasars: absorption lines Supporting material: figure set, machine-readable tables

1. Introduction

One of the major questions driving studies of galaxy evolution is the nature of the interaction between galaxies and their central supermassive black holes (SMBHs). A possible avenue for this interaction is through quasar outflows, or winds, generated near the SMBH (e.g., Di Matteo et al. 2005; Moll et al. 2007; King & Pounds 2015). Quasar outflows are launched from the accretion disk around the SMBH (e.g., Murray et al. 1995; Proga 2000; Baskin et al. 2014; Higginbottom et al. 2014), and are thought to regulate the growth of the host galaxy, as well as the SMBH itself, through the process of AGN feedback. Specifically, outflows provide a mechanism for a host galaxy to evacuate or compress gas, slowing SMBH accretion and suppressing or enhancing hostgalaxy star formation. Understanding the physical properties of these outflows is thus integral to developing models of galaxy evolution. In the context of rest-frame UV quasar spectra, these outflows manifest themselves most prominently as broad absorption lines (BALs), features that exhibit observed velocity widths on the scale of several thousand km s⁻¹ (Weymann et al. 1991). BALs are an extremely useful probe of the physical properties of outflows as well as the environments from which they originate.

Previous studies have demonstrated that BALs are significantly variable, both in strength and in shape (e.g., Barlow 1993; Lundgren et al. 2007; Gibson et al. 2008; Capellupo et al. 2013; Filiz Ak et al. 2013; He et al. 2015; Wang et al. 2015). Proposed mechanisms for BAL variability include inhomogeneous emission, ionization-state changes, and "cloud crossing," which refers to the drift of absorbing gas across the line of sight (e.g., Hall et al. 2007; Capellupo et al. 2013; Filiz Ak et al. 2013; He et al. 2017). Characterizing the BAL variations can yield constraints for many physical properties of quasar outflows; for example, ionization-state changes and cloud-crossing allow an inference of the density and/or radial distance of relevant gas from the SMBH (e.g., Capellupo et al. 2013).

While BAL variability has been commonly studied on restframe timescales of years and months (e.g., Gibson et al. 2010), observations probing timescales of days and hours are rare (e.g., Capellupo et al. 2013; Grier et al. 2015). Moreover, most studies have suffered a trade-off between the number of observed quasars and the number of epochs. For this reason, there has not yet been a study with both the sample size and rapid cadence required to make robust statistical statements about variability on timescales on the order of days to hours in the quasar rest frame. Table 1 presents various sample characteristics of several prior BAL-variability studies for the purpose of comparison to this investigation.

¹¹ Alfred P. Sloan Research Fellow.

Table 1Parameters of Various BAL Variability Studies

Reference	No. of Quasars	N _{epochs} ^a Range	Median $N_{\rm epochs}^{\ \ a}$	Δt ^b Range (days)	Median $\Delta t^{\rm b}$ (days)	Redshift Range	Median Redshift
Barlow (1993)	23	2–6	•••	73–440	•••	•••	
Lundgren et al. (2007)	29	2	2	18-121	81	1.70-3.26	2.00
Gibson et al. (2008)	13	2	2	1100-2200	1500	1.72-2.81	2.02
Gibson et al. (2010)	14	2–4	3	15-2500	1100	2.08-2.89	2.41
Capellupo et al. (2011)	24	2–4	4	130-2800	1600	1.22-2.91	2.23
Capellupo et al. (2012)	24	2-10	5	15-3000	270	1.22-2.91	2.23
Vivek et al. (2012)	5	4–14	5	3.7-1200	140	0.81 - 1.97	1.23
Haggard et al. (2012)	17	6	•••	0.37-330			
Filiz Ak et al. (2012)	19	2–4	2	400-1400	730	1.71-2.57	2.00
Capellupo et al. (2013)	24	2-13	7	7.3-3200	270	1.22-2.91	2.23
Filiz Ak et al. (2013)	291	2-12	2	0.22-1350	770	2.00-3.93	2.55
Welling et al. (2014)	46	2–6	2	80-6000	500	0.24-3.46	2.21
Filiz Ak et al. (2014)	671	2	2	310-1500	930	1.90-3.83	2.28
Vivek et al. (2014)	22	3–7	5	10-2800	280	0.20-2.10	1.28
He et al. (2015)	188	2	2	3-1000	250	1.70-4.10	2.18
Wang et al. (2015)	452	2-30	4	1-1800	260	2.20-4.70	2.25
Vivek et al. (2016)	50	2–5	2	800-2000	1100	1.65-2.90	1.96
He et al. (2017)	843	2-40	5	1-2500	280	1.90-4.70	2.21
Rogerson et al. (2018)	105	3–7	3	1.8-1210	800	1.68-4.13	2.51
This work	27	3–68	58	0.21-250	2.4	1.62-3.72	2.35

Notes

Spectroscopic data from the Sloan Digital Sky Survey Reverberation Mapping project (SDSS-RM) (Shen et al. 2015) provide a novel opportunity to investigate BAL variability in a representative sample of quasars using many epochs of spectra on shorter timescales than have previously been explored. The SDSS-RM project is an ongoing reverberation-mapping campaign that began in 2014 and has continued to obtain data in subsequent years during January-July of each year. Many quasars in the SDSS-RM quasar sample exhibit BAL features. Prior to this program, the shortest BAL-variability timescales probed were on the order of 8–10 days (Capellupo et al. 2013). However, with the rapid cadence of the SDSS-RM data set, Grier et al. (2015) were able to investigate even shorter timescales: They identified significant variability of a C IV BAL on timescales as short as 1.2 days in the quasar rest frame. On these short timescales, the equivalent width (EW) of this BAL varied by roughly 10%. Because the BAL showed little variability in shape, Grier et al. (2015) proposed that this feature was likely varying via ionizationstate changes in the absorbing medium. This discovery of such short-timescale BAL variability motivates subsequent investigations to determine whether this variability is common among BAL quasars.

In this work, we present the results of a search for short-timescale variability within a sample of BAL quasars using data from the SDSS-RM project. The goals of this study are to determine the frequency of short-timescale BAL variability, provide insights into quasar-wind variability mechanisms, and further constrain quasar-wind properties in BAL quasars exhibiting significant short-timescale variability. Section 2 presents the SDSS-RM observations and characterizes our quasar sample. Section 3 describes data processing, the measured BAL parameters such as EWs, mean depths, and centroid velocities, and our criteria for selecting robust cases of BAL variability. Section 4 discusses our results, our

examination of coordinated variability, physical constraints calculated from our measurements, and the implications of our work. Section 5 summarizes our findings and elaborates on feasible future work in regards to short-timescale BAL variability studies. Where necessary, we adopt a cosmology with $H_0=70~{\rm km~s^{-1}~Mpc^{-1}},\,\Omega_M=0.3,$ and $\Omega_\Lambda=0.7.$

2. Observations and Data Preparation

2.1. SDSS-RM Observations

In 2014, SDSS-RM obtained 32 epochs of spectra of 849 quasars using the Baryon Oscillation Spectroscopic Survey (BOSS) (Eisenstein et al. 2011; Dawson et al. 2013) spectrograph on the SDSS 2.5 m telescope (Gunn et al. 2006; Smee et al. 2013); 12–13 additional epochs per year were taken subsequently in 2015, 2016, and 2017 as a part of the SDSS-IV eBOSS program (Dawson et al. 2016; Blanton et al. 2017), yielding 69 total epochs of spectroscopy over the four years. The BOSS spectrograph covers a wavelength range of $3650-10,400\,\text{Å}$ and has a spectral resolution of R=2000 with a field of view that is 3° in diameter. At the beginning of the SDSS-RM program, all 849 quasars were assigned numerical identifiers based upon their position on the spectrograph plate—we hereafter refer to these identifiers as RM IDs and refer to all quasars by this designation.

2.2. Initial Quasar Sample

We began with a parent sample of 94 quasars in the SDSS-RM sample that were identified to likely host prominent C IV absorption features, each with 69 epochs of data from the four years of SDSS-RM monitoring. This initial sample was chosen by visual inspection and thus may contain C IV absorbers that do not meet the formal requirements for BALs (e.g., Weymann et al. 1991). We later refine our sample to include only formally

^a N_{epochs} refers to the number of epochs per quasar.

^b Δt is measured in the quasar rest frame.

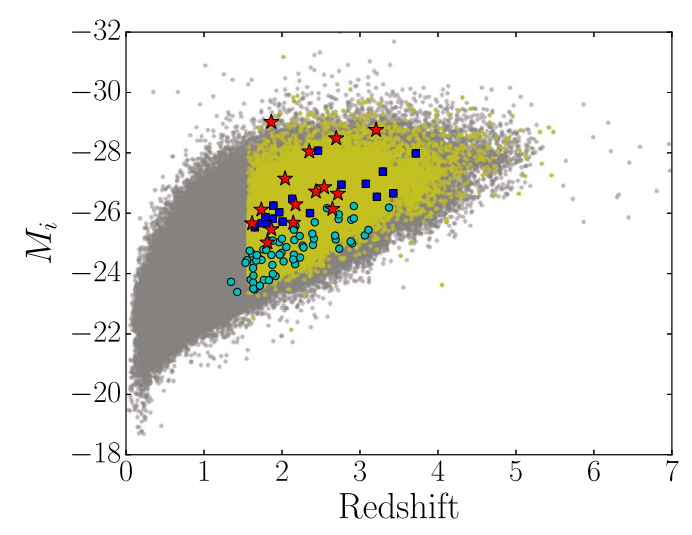


Figure 1. Absolute *i*-magnitude as a function of redshift. Gray and yellow points show non-BAL and C IV-BAL quasars from the DR14 quasar catalog (Pâris et al. 2018), respectively. Cyan circles represent quasars in our initial 94 object sample that were cut due to low SN; blue squares show the quasars in our final sample that show no significant short-timescale (<10 day) variability, and red stars indicate our 15 quasars that show significant short-timescale variability. Data for the SDSS-RM quasars were retrieved from Y. Shen et al. (2018, in preparation). All absolute magnitudes have been corrected to $M_i[z=2]$, following Richards et al. (2006).

detected BALs; see Section 3.1. Figure 1 shows the absolute magnitude-redshift distribution of our parent quasar sample compared to the general population of quasars from the DR14 quasar catalog (Pâris et al. 2018). The quasars in our parent sample are typical of BAL quasars within the magnitude/redshift plane.

2.3. Data Preparation

The SDSS-RM data were first processed using the standard BOSS spectroscopic reduction pipeline; however, to further improve the spectrophotometric flux calibrations of the data, a custom flux calibration scheme was applied (Shen et al. 2015). We then corrected the spectra for Galactic extinction using an $R_{\rm V}=3.1$ Milky Way extinction model (Cardelli et al. 1989) and $A_{\rm V}$ values from Schlafly & Finkbeiner (2011).

We searched for pixels with poor sky-subtraction residuals using the SDSS bitmask flag "BRIGHTSKY" and linearly interpolated over these pixels. This process suppressed much of the spectral mid-optical sky contamination, although significant sky contamination residuals are still visible at the far red and blue ends of the spectra. A few spectra contained additional bad pixels that were not flagged during the SDSS data reduction process. These pixels appeared as dramatic spikes or dips in flux—we manually removed these points and linearly interpolated over the region for ease of spectra visualization. Before continuing our analysis, we translated the wavelengths of the spectra into the quasar rest frame using systemic redshifts from Shen et al. (2016). We adopt these redshift measurements for the remainder of this investigation. To remove the aforementioned sky contamination that was often present at the edges of the spectra, we cropped them to cover roughly the wavelength regions spanning 1200-2600 Å in the quasar rest frame.

During the course of our study, we identified an issue with the SDSS eBOSS DR14 pipeline reductions that produced wavelength-dependent residuals in data processed after 2014.

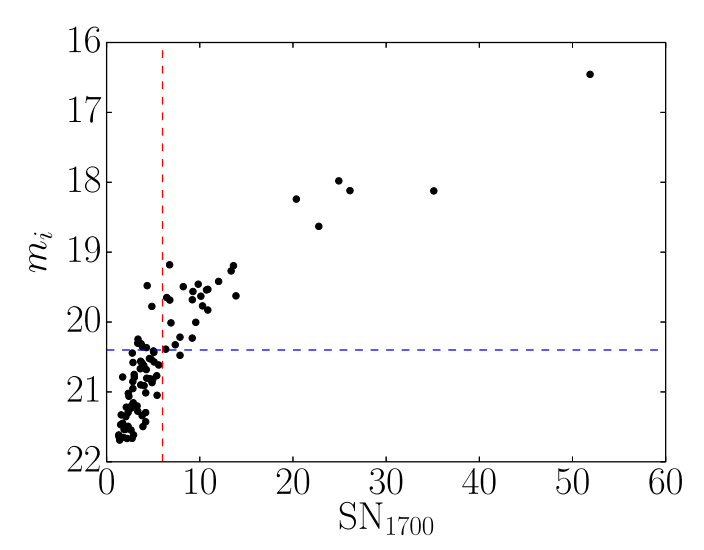


Figure 2. Quasar apparent *i*-magnitude (m_i) vs. median SN_{1700} for the entire SDSS-RM BAL parent sample. The dashed blue line represents the location of our *i*-magnitude limit, and the dashed vertical red line shows the SN_{1700} cut. We note, however, that the SN_{1700} cut was made on individual spectral epochs, while the figure includes the median SN_{1700} of all spectra for each quasar.

The residuals resulted from incorrect background estimation in the presence of nearby standard stars. Spectra are grouped in bundles of 20 fibers on the detectors, and the DR14 background estimation used a new scheme to measure the background flux within these bundles. This issue has since been fixed in more recent versions of the pipeline reductions; however, it was not yet resolved while we were carrying out the bulk of our analysis. Empirically, we found that excluding fibers from bundles including two or more standard stars removed all fibers with obvious spectral residuals. Our team thus identified the spectra from fibers in these bundles at each epoch in our sample and removed these individual spectra from our sample to avoid introducing resultant systematic uncertainties. Eighteen of the quasars in our sample had at least one epoch that was eliminated. For some of these quasars, only a single epoch was removed (e.g., RM 770), while in others, all of the post-2014 epochs were removed (e.g., RM 786).

2.4. Magnitude and Signal-to-noise Cuts

Our goal is to construct a sample that is representative of the general BAL quasar population, so we make only two simple cuts to our sample. Because we are searching for smallamplitude BAL variability, we require our spectra to have reasonably high signal-to-noise ratios (SN) near the C IV region of the spectrum. To quantify the SN, we measure SN_{1700} , defined as the median SN of the pixels in the 1650-1750 Å region in the quasar rest frame. We follow previous work (e.g., Gibson et al. 2009a) and require our objects to have SN_{1700} of 6 or higher per pixel (reduced SDSS spectra have a resolution of $69 \,\mathrm{km \, s^{-1}}$ per pixel). To achieve this, we selected only quasars with *i*-band magnitudes $m_i < 20.4$, which mostly eliminated quasars with SN_{1700} lower than this threshold (see Figure 2). This m_i constraint restricted the sample to 36 objects. Figure 2 displays m_i versus the median SN_{1700} calculated from all observed epochs for each quasar.

Even after this magnitude cut, individual epochs of some objects had fairly low SN due to variations in observing conditions. Often, a reliable continuum fit was difficult to

Table 2
Final Quasar Sample Information

SDSS ID	RM ID	R.A. ^a (deg)	Decl. ^a (deg)	z ^a	$m_i^{\mathbf{a}}$	SN ₁₇₀₀	$N_{ m epochs}$	$\Delta t_{ m rest}$ (days)	Continuum Fit ^b	Emission- Line Fit ^c
J141607.12+531904.8	RM 039	214.02967	53.31800	3.08	19.77	10.24	58	2.88	R	V
J141741.72+530519.0	RM 073	214.42385	53.08863	3.43	20.37	6.76	3	7.34	R	DG
J141432.46+523154.5	RM 116	213.63526	52.53182	1.88	19.68	9.50	64	3.99	R	DG
J141103.17+531551.3	RM 128	212.76324	53.26426	1.86	20.01	7.25	50	3.60	R	V
J141123.68+532845.7	RM 155	212.84871	53.47936	1.65	19.65	7.14	41	2.61	R	DG
J141935.58+525710.7	RM 195	214.89825	52.95297	3.22	20.33	7.66	59	2.75	R	DG
J141000.68+532156.1	RM 217	212.50287	53.36560	1.81	20.39	7.12	41	2.46	R	V
J140931.90+532302.2	RM 257	212.38295	53.38395	2.43	19.54	10.88	65	3.02	U	V
J141927.35+533727.7	RM 284	214.86398	53.62436	2.36	20.22	8.16	63	3.46	U	GH
J142014.84+533609.0	RM 339	215.06184	53.60252	2.01	20.00	9.68	64	3.47	R	DG
J141955.27+522741.1	RM 357	214.98029	52.46144	2.14	20.23	9.25	65	3.49	R	DG
J142100.22+524342.3	RM 361	215.25092	52.72844	1.62	19.46	9.92	66	3.94	R	V
J141409.85+520137.2	RM 408	213.54107	52.02702	1.74	19.63	10.27	65	4.00	R	DG
J142129.40+522752.0	RM 508	215.37253	52.46445	3.21	18.12	35.09	69	2.21	R	DG
J142233.74+525219.8	RM 509	215.64060	52.87219	2.65	20.30	6.51	10	3.84	R	V
J142306.05+531529.0	RM 564	215.77521	53.25807	2.46	18.24	20.36	67	2.69	U	DG
J140634.14+525407.8	RM 565	211.64227	52.90219	1.79	19.48	6.25	3	13.78	U	V
J141007.73+541203.4	RM 613	212.53224	54.20095	2.35	18.12	26.18	68	2.87	R	V
J140554.87+530323.5	RM 631	211.47865	53.05655	2.72	19.83	11.28	65	2.79	R	GH
J141648.26+542900.9	RM 717	214.20109	54.48360	2.17	19.69	7.18	49	3.74	R	DG
J142419.18+531750.6	RM 722	216.07996	53.29739	2.54	19.49	8.65	59	3.10	U	DG
J142404.67+532949.3	RM 729	216.01946	53.49704	2.76	19.56	9.66	63	2.91	R	V
J142225.03+535901.7	RM 730	215.60432	53.98381	2.69	17.98	24.74	65	2.81	R	GH
J142405.10+533206.3	RM 743	216.02126	53.53509	1.74	19.18	6.97	49	3.47	R	DG
J142106.86+533745.2	RM 770	215.27862	53.62923	1.86	16.46	51.89	69	3.25	R	DG
J141322.43+523249.7	RM 785	213.34349	52.54715	3.72	19.19	13.81	67	2.11	U	GH
J141421.53+522940.1	RM 786	213.58974	52.49447	2.04	18.63	22.96	68	3.17	R	None

Notes.

(This table is available in machine-readable form.)

obtain for these epochs, rendering further measurements difficult or impossible. Therefore, we impose a subsequent $\mathrm{SN}_{1700} \geqslant 6$ cut on each individual spectral epoch to remove epochs where reliable fits were unobtainable due to low SN. For some quasars, this removed an epoch or two from our sample, while in four cases, all observations of the given quasar were dropped. There is some scatter in the relationship between m_i and SN_{1700} , and these four objects fell below our SN threshold despite our m_i cut; see Figure 2. Imposing this SN_{1700} limit yielded 32 quasars that potentially host C IV BALs and have sufficient SN for reliable analysis.

2.5. Continuum and Emission-line Fitting

We follow previous BAL-variability studies (e.g., Filiz Ak et al. 2012, 2013; Grier et al. 2015, 2016) and use a least-squares fitting algorithm to fit reddened power laws to all spectra using the SMC-like reddening model of Pei (1992). We began the fitting process by adopting the relatively line-free (RLF) regions determined by Gibson et al. (2009b), with a few revisions made after consulting the composite quasar spectra published by Vanden Berk et al. (2001) to identify regions relatively free of emission or absorption. Most quasars required

additional deviations from the Gibson et al. (2009b) regions for optimal continuum fits due to the presence of strong absorption or emission within these regions. For a given quasar, we adopted the same RLF fit regions for all epochs. Because we manually adjusted the line-free regions, we did not need to utilize the sigma clipping techniques commonly employed by previous investigations. (e.g., Filiz Ak et al. 2013.) One epoch of one quasar (RM 284, MJD 57451) was missing sections of the spectrum toward the red end, causing difficulties with the continuum fits; we exclude this epoch from our analysis, as the missing pixels left us unable to obtain a reasonable fit.

For some spectra, the best-fit power law was consistent with no reddening, so we adopted a simple power law for our continuum—our choices of reddened or unreddened fits are indicated for each quasar in Table 2. Uncertainties in the continuum fits were determined using Monte Carlo methods; the flux values of each pixel within the fitting region were altered by a random Gaussian deviate scaled to the pixel uncertainties, and the spectra were subsequently refit. Our continuum fits to the mean spectra created from the 2014 observations are presented in Figure 3.

Several quasars exhibited BALs at velocities insufficient to separate them cleanly from the C IV emission line. To remove

^a J2000 Position, redshift, and magnitude measurements were obtained from SDSS Data Release 10 (Ahn et al. 2014). The *i*-magnitudes provided are point-spread function magnitudes that have not been corrected for Galactic extinction.

^b A designation of "R" indicates that a reddened power-law continuum fit was used for this quasar, and a designation of "U" indicates the use of an unreddened power law.
^c A designation of "V" indicates that a Voigt profile to was used to represent the C IV emission line, "DG" indicates the use of a double-Gaussian profile, "GH" indicates a Gauss-Hermite profile was used, and "None" indicates that we were unable to obtain any acceptable emission-line fit, so the continuum-only fit was adopted.

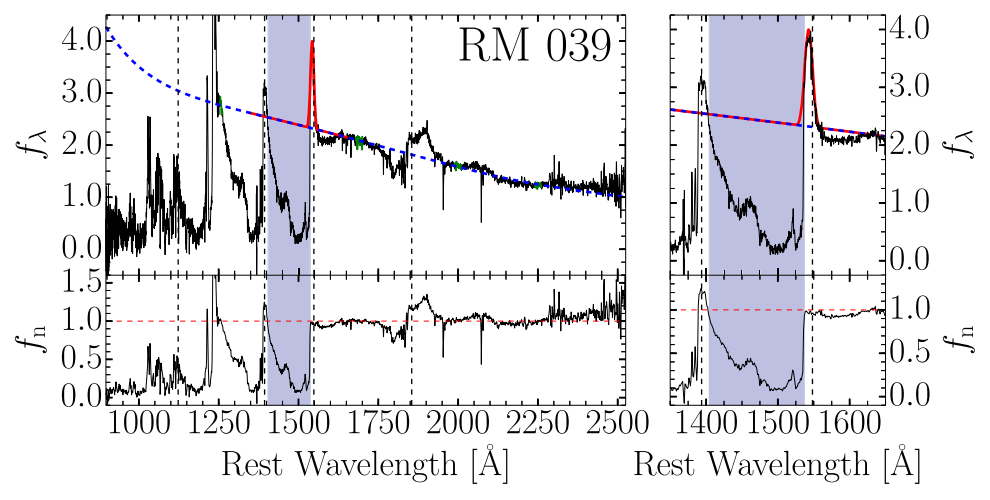


Figure 3. The mean spectrum of quasar RM 039, generated from data taken by the SDSS-RM project in 2014. The top subpanels show the quasar flux density, and the bottom subpanels show the continuum+emission-line-normalized fluxes f_n . The left subpanels show the entire spectrum, while the right subpanels display only the C IV region. Thick dashed blue lines represent the continuum fits, solid red lines show our C IV emission-line fits, and green regions show the adopted continuum regions used in the continuum fits. Shaded regions indicate the C IV BALs identified in each object. The horizontal red dashed lines in the bottom subpanels mark a normalized flux of 1.0 to guide the eye. Vertical black dotted lines indicate the rest-frame wavelengths of various species of interest: P V (1115 Å), Si IV (1393.8 Å), C IV (1548.2 Å), and Al III (1854.7 Å). f_{λ} has units of 10^{-17} erg s⁻¹ cm⁻² Å⁻¹. (The complete figure set (27 images) is available.)

emission-line contamination from the BAL features, we follow Grier et al. (2015) and fit Gauss-Hermite (van der Marel & Franx 1993), double-Gaussian (Park et al. 2013), and Voigt profile (Gibson et al. 2009b) models to the C IV emission line. To do this, we constructed mean spectra for each individual year of the campaign for each object from all epochs passing our SN₁₇₀₀ threshold criterion defined in Section 2.4. For each object, we choose the best-fit model (Gauss-Hermite, double-Gaussian, or Voigt), based on visual inspection; the chosen models for each quasar are listed in Table 2. We adopt the fit parameters from the mean spectrum (except the amplitude parameter) for all epochs in a given year (i.e., the 2014 mean spectrum fit parameters were used for all 2014 SDSS-RM epochs, etc.). We then fit the emission lines to each individual epoch while treating only the amplitude as a free parameter. This process assumes that only the amplitude of the emission lines varied within the same observing season and all other characteristics (e.g., widths, centers, etc.) remained constant. Our emission-line fits are displayed in Figure 3. We add the continuum and emission-line fits together, hereafter referred to as the "continuum+emission-line" fits.

3. Final Sample Selection and BAL Measurements

3.1. Final BAL Quasar Sample

We are primarily interested in quasars that host C IV BALs at the beginning of the SDSS-RM campaign. To identify such BALs, we first binned all of the 2014 mean normalized spectra by three pixels to account for SDSS oversampling of the spectral line function. Binning ensures that neighboring pixels are almost entirely uncorrelated. We then smoothed the binned spectra by three pixels to reduce noise. We note that smoothing was used only for the BAL search; we perform all additional measurements on the unsmoothed, binned spectra. We then searched each of the 2014 mean spectra for regions in which the normalized flux density drops below 0.9 for velocity widths greater than 2000 km s⁻¹ (i.e., a BAL exists that is consistent with the formal definition of Weymann et al. 1991). We

restricted our search to within 30,000 km s⁻¹ blueward of the adopted C IV rest wavelength (1548.202 Å) and include BALs that extend redward of the C IV rest wavelength by up to 1000 km s⁻¹. Quasars without formal C IV BALs in their 2014 mean spectra, such as those containing only mini-BALs or those for which a BAL did not appear until later on in the campaign, were dropped from our sample.

After identifying the BALs, we visually inspected all spectra to ensure no BALs were contaminated by residual sky flux or bad pixels. Three BALs were found to either have bad pixels within the BAL trough (in quasars RM 528 and RM 729) or to contain residual sky lines within the BAL (RM 195) that could potentially affect our analysis. These features were not detected by the SDSS pipeline, and they affect BALs with an unfortunate combination of velocity and quasar redshift. We excluded these BALs from our sample. This resulted in the removal of RM 528 from our sample, as this quasar possessed only the contaminated BAL. The other two quasars harbor additional uncontaminated BALs, so they remain in our final sample.

The final sample contains 27 quasars that have 37 uncontaminated C IV BALs between them. We present various characteristics of the quasars in our final BAL quasar sample in Table 2 and provide information on each individual identified BAL in Table 3. To distinguish between C IV BALs when a spectrum has more than one present, we assign identifiers [A] and [B] to the BALs as wavelength increases (and as velocity decreases); therefore, in cases with multiple BALs, [A] refers to the higher-velocity BAL, and [B] to the lower-velocity BAL. None of our quasars contained more than two C IV BALs. The regions of the spectra containing C IV BALs in each quasar are highlighted in Figure 3.

Our final sample of BAL quasars does not generally have properties different from those of the larger BAL-quasar population (see Figure 1). Most (26 out of 27) of the quasars in our sample are radio-quiet and are undetected by the FIRST radio survey (White et al. 1997; compiled by Shen et al. 2018). The one exception is RM 155, which has a measured radio-loudness parameter of R = 42.89; R is defined as the

Table 3
CIV BAL Measurements from 2014 Mean Spectra

RM ID	BAL ID	$v_{ m max}^{-a}$	$v_{ m min}^{a}$	$v_{\rm cent}^{-a}$	$\langle d angle$	EW (Å)	FA14 ID ^b	P V ^c
RM 039	A	29148	2190	13445	0.67	88.5 ± 0.7	CIV _{SA}	Y
RM 073	A	10142	5768	7821	0.23	5.1 ± 0.4	CIV ₀₀	N
RM 073	В	4586	1456	2680	0.51	8.0 ± 0.2	CIV ₀₀	N
RM 116	A	11599	5467	7946	0.26	8.2 ± 0.3	CIV _{S0}	
RM 116	В	4860	2746	3650	0.36	4.0 ± 0.2	CIV ₀₀	
RM 128	A	21360	4814	10569	0.38	31.5 ± 0.7	CIV_{S0}	
RM 128	В	2691	583	1486	0.22	2.5 ± 0.2	CIV ₀₀	
RM 155	A	7670	447	3249	0.54	19.9 ± 0.4	CIV_{SA}	
RM 195	A	3243	378	1788	0.41	5.9 ± 0.1	CIV ₀₀	N
RM 217	A	19323	14820	17014	0.19	4.2 ± 0.4	CIV_{S0}	
RM 217	В	11640	2901	6379	0.47	20.8 ± 0.5	CIV _{S0}	
RM 257	A	24762	6659	13586	0.48	42.6 ± 0.4	CIV_{SA}	Y
RM 257	В	4117	2098	3067	0.50	5.2 ± 0.1	CIV ₀₀	N
RM 284	A	24141	19496	21736	0.12	2.8 ± 0.2	CIV _{N0}	
RM 339	A	15188	7789	10850	0.26	9.7 ± 0.3	CIV_{SA}	
RM 357	A	14782	11935	13284	0.15	2.2 ± 0.3	CIV ₀₀	
RM 357	В	7152	1891	3934	0.53	14.1 ± 0.3	CIV_{S0}	
RM 361	A	7122	1463	3980	0.54	15.3 ± 0.3	CIV _{N0}	
RM 408	A	4451	656	2201	0.50	9.8 ± 0.2	CIV ₀₀	
RM 508	A	21344	18101	19590	0.36	5.7 ± 0.1	CIV ₀₀	N
RM 509	A	24553	13814	18176	0.26	13.6 ± 0.5	CIV_{S0}	N
RM 509	В	2464	337	1371	0.46	5.1 ± 0.1	CIV ₀₀	N
RM 564	A	25282	21819	23559	0.17	2.8 ± 0.1	CIV_{S0}	
RM 565	A	27794	14010	20647	0.21	13.7 ± 1.3	CIV _{N0}	
RM 565	В	13688	3878	8127	0.24	11.7 ± 1.0	CIV_{S0}	
RM 613	A	20046	15713	17872	0.22	4.8 ± 0.2	CIV ₀₀	
RM 631	A	8931	5858	7295	0.47	7.2 ± 0.2	CIV_{S0}	Y
RM 717	A	23343	8567	15064	0.30	21.8 ± 0.7	CIV _{S0}	
RM 722	A	6238	2063	3955	0.58	12.5 ± 0.2	CIV ₀₀	N
RM 729	A	9754	3465	6306	0.37	11.8 ± 0.3	CIV _{S0}	Y
RM 730	A	27969	15310	22035	0.40	24.5 ± 0.2	CIV _{S0}	Y
RM 730	В	14823	11675	12893	0.15	2.5 ± 0.1	CIV ₀₀	N
RM 743	A	11177	4423	7402	0.31	10.6 ± 0.6	CIV _{SA}	
RM 770	A	20663	15904	18231	0.15	3.6 ± 0.1	CIV ₀₀	
RM 785	A	26858	12732	19713	0.21	14.3 ± 0.3	CIV _{S0}	Y
RM 786	A	14967	11437	13062	0.15	2.7 ± 0.2	CIV ₀₀	
RM 786	В	8814	-338	3456	0.75	34.4 ± 0.2	CIV _{SA}	

Notes.

(This table is available in machine-readable form.)

ratio of fluxes at rest frame 6 cm and 2500 $\rm \mathring{A}$ (e.g., Shen et al. 2018).

Our final sample of spectra has a median of 58 epochs per object; this is the highest of any BAL variability study by almost a factor of 10 (see Table 1). Epochs separated by rest-frame timescales (hereafter referred to as $\Delta t_{\rm rest}$) on the order of a single day are frequent. Hereafter, we refer to all variability on timescales of less than 10 days in the quasar rest frame as "short-timescale" or "rapid" variability. The median rest-frame time resolution of the SDSS-RM observations among our sample of quasars is 2.4 days, nearly a factor of 10 lower than even the shortest-timescale studies previously reported (see Table 1). Our sample spans a redshift range of 1.62–3.72, which is comparable to previous studies. This is by necessity,

as the C IV region must be redshifted to within the range of spectral coverage of the instruments used in each study. Figure 4 displays the distribution of $\Delta t_{\rm rest}$ between all pairs of subsequent epochs for the sample, including only sequential pairs of epochs for each quasar that are separated by less than 10 days in the quasar rest frame.

3.2. BAL Measurements

After identifying the BALs and refining the BAL sample, we calculated the BAL velocity bounds (v_{\min} and v_{\max}) from the pixels on either end of the trough that recovered to normalized flux densities of 0.9 or higher. We measure these velocity bounds from the mean spectrum created from the data taken in

^a Velocities are in units of km s⁻¹.

^b BAL designation according to whether or not BALs or mini-BALs are present for Si IV and Al III, as defined by Filiz Ak et al. (2014); see Section 4.3.3. A designation of C IV_{N0} indicates that the Si IV line is not completely covered by our spectrum at those velocities or we are unable to otherwise determine whether or not it is present, so we are unsure of the designation.

^c This column indicates whether or not there is a suspected corresponding P V BAL or mini-BAL (see Section 4.3.3): "Y" indicates that P V is suspected to be present; "N" indicates that it is not. Entries with no data indicate that the P V region is not covered by the SDSS spectra.

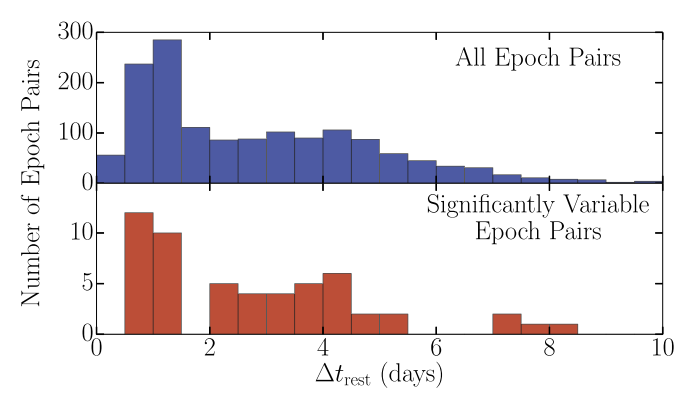


Figure 4. Histogram of the rest-frame time difference $\Delta t_{\rm rest}$ distribution of our sample. The top subpanel displays the distribution of our entire 27 object sample; the bottom subpanel displays only that of epoch pairs exhibiting significant short-timescale variability (see Section 3.3). The region $\Delta t_{\rm rest} < 2$ days is well-populated.

2014 for each quasar and adopt them for all individual epochs. We define our velocity ranges as positive and increasing at larger blueshifts. We computed the rest-frame EWs for each BAL, along with rest-frame mean fractional depth $\langle d \rangle$ and absorbed-flux weighted centroid velocity ($\nu_{\rm cent}$). The EW and $\nu_{\rm cent}$ are defined as follows:

$$EW = \int_{\lambda_{min}}^{\lambda_{max}} \left[1 - f_{n}(\lambda) \right] d\lambda \tag{1}$$

$$v_{\text{cent}} = \frac{\int_{v_{\text{min}}}^{v_{\text{max}}} v[1 - f_{\text{n}}(v)] dv}{\int_{v_{\text{min}}}^{v_{\text{max}}} [1 - f_{\text{n}}(v)] dv}$$
(2)

where f_n is the continuum+emission-line-normalized flux across the BAL trough. We propagate the normalized spectral uncertainties to determine the uncertainty in our EW measurements. We provide these measurements from the 2014 mean spectra for our final sample in Table 3, and provide measurements for each individual epoch in Table 4. The EW measurements of each BAL as a function of the Modified Julian Date (MJD) are presented in Figure 5. Nearly all of our BALs show significant variability over the four years of monitoring—most of the EW light curves reveal visible trends across even single observing seasons.

3.3. Detection of Significant Variability

We began our investigation into BAL variability by measuring ΔEW , the change in EW of the BAL between two subsequent epochs. We calculated the uncertainty in the ΔEW parameter using a quadrature sum of EW uncertainties from each epoch of interest. As discussed above, we removed some epochs from our sample due to various issues (low SN, bad sky subtraction, etc.); therefore, from object to object, the cadence deviates from the SDSS-RM observation cadence. Figure 6 shows the distribution of ΔEW for all sequential epoch pairs in our sample. The distribution of ΔEW is centered on zero and contains mostly small-amplitude variations, though there are rare cases of more dramatic variability, particularly on timescales ranging from 10 to 100 days in the quasar rest frame.

To identify significant variability between epoch pairs, we follow previous works (e.g., Grier et al. 2015) and require that

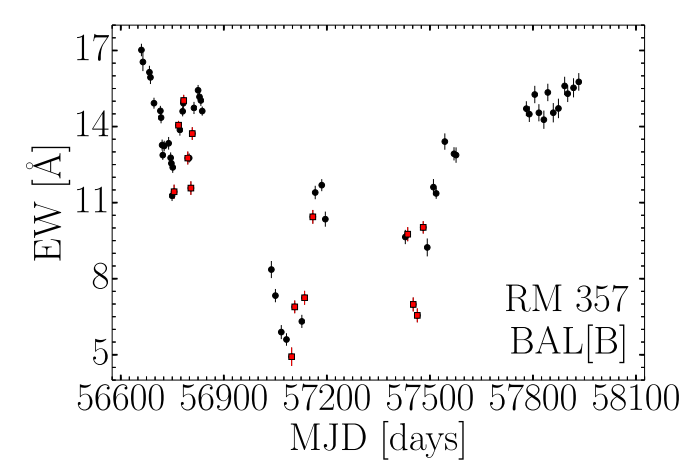


Figure 5. EW vs. MJD for RM 357 BAL[B]. Epoch pairs that satisfy our criteria for significant short-term variability (see Section 3.3) are marked by red squares.

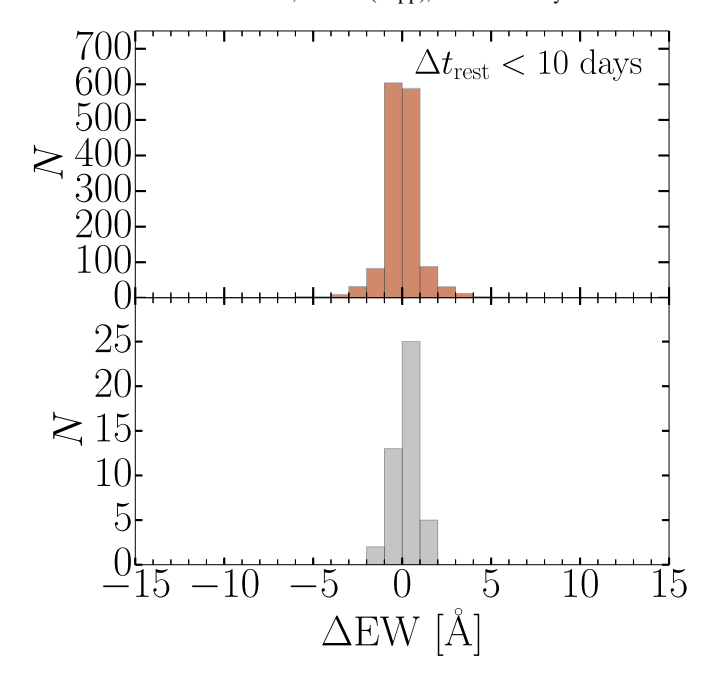
(The complete figure set (37 images) is available.)

Table 4
C IV BAL Measurements per Epoch

RM ID	BAL ID	MJD (days)	(km s^{-1})	$\langle d \rangle$	EW (Å)
RM 039	A	56660.21	13250	0.65	85.7 ± 0.8
RM 039	A	56664.51	13320	0.63	83.8 ± 1.0
RM 039	A	56683.48	13260	0.66	88.0 ± 0.8
RM 039	A	56686.47	13230	0.66	87.6 ± 0.8
RM 039	A	56696.78	13390	0.68	89.5 ± 0.9
RM 039	A	56715.39	13200	0.67	88.6 ± 0.7
RM 039	A	56717.33	13440	0.65	86.1 ± 0.6
RM 039	A	56720.45	13380	0.65	86.6 ± 0.7
RM 039	A	56722.39	13310	0.66	87.2 ± 0.5
RM 039	A	56726.46	13270	0.63	83.6 ± 0.6
RM 039	A	56739.41	13470	0.67	89.0 ± 0.6
RM 039	A	56745.28	13530	0.67	89.4 ± 0.6
RM 039	A	56747.42	13850	0.65	86.4 ± 0.8
RM 039	A	56749.37	13480	0.67	88.9 ± 0.7
RM 039	A	56751.34	13520	0.65	86.0 ± 0.7
RM 039	A	56755.34	13560	0.67	89.1 ± 0.8
RM 039	A	56768.23	13590	0.67	89.0 ± 0.6
RM 039	A	56772.23	13470	0.67	88.9 ± 0.5

(This table is available in its entirety in machine-readable form.)

the ratio of ΔEW to its uncertainty, $\sigma_{\Delta EW}$, be at least four (i.e., we impose a 4σ significance requirement on ΔEW). However, solely relying on the aforementioned significance criteria returned several cases of supposed BAL variability for which nearby regions outside the BAL also varied considerably. This phenomenon suggests that the variability observed within the BAL may be due to spectral variability unassociated with the BAL itself (whether real deviations from a power law, or spurious due to spectrophotometric residuals on scales of tens of Å), or inconsistencies in continuum fits. These inconsistencies are likely due to nearby emission-line variability or a lack of line-free regions close to the BAL, which, combined with noise, causes the continuum fits to vary somewhat from epoch to epoch. Such cases motivated the implementation of additional criteria that could isolate true BAL variability from variations in continuum and emission-line fits. For these



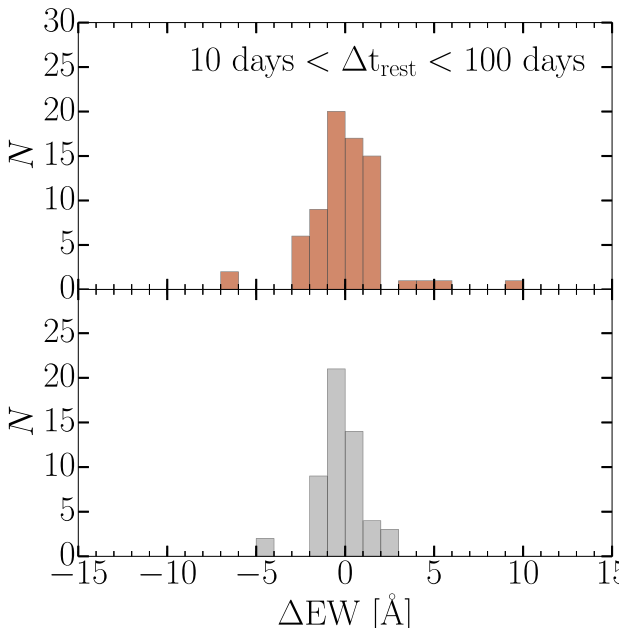


Figure 6. The distribution of ΔEW among BAL quasars. Panels with red histograms show measurements from our work using all pairs of sequential epochs for each quasar in our sample. Panels with gray histograms represent data from Barlow (1993), Lundgren et al. (2007), Gibson et al. (2008), and Filiz Ak et al. (2013). The top two panels show the distributions for epochs that are separated by 0–10 days in the quasar rest frame and the bottom two panels show the distributions for epochs separated by 10–100 days in the quasar rest frame. See Section 4.2 for a comparison between our work and previous studies.

purposes, we define a quantity hereafter referred to as G:

$$G = \frac{\chi^2 - (N-1)}{\sqrt{2(N-1)}} \tag{3}$$

where the χ^2 quantity is the square of the difference between fluxes at two spectral epochs divided by their combined uncertainty, summed over the N pixels within a specified

region. The expected value and standard deviation of the distribution of the χ^2 statistic for a region of N pixels are N-1 and $\sqrt{2(N-1)}$, respectively; thus, the G statistic should have a mean of zero and standard deviation of one if there are no variations between the two spectra. Larger absolute values of G indicate inconsistencies between the two spectra, suggesting variability at some level of significance.

For each BAL, we located nearby regions that contained very few features, hereafter referred to as "continuum" regions. We use these regions to search for cases where there is variability within the BAL region of the normalized spectra but *not* within the continuum regions. Because we did not fit the nearby Si IV emission line, this region (and all regions blueward) were not included in the continuum regions. Continuum regions redward of Si IV were selected via visual inspection, referencing the composite quasar spectra of Vanden Berk et al. (2001) to search for wavelength regions with minimal contaminants. We then calculated the G values in the identified continuum regions and within the BAL region. Hereafter, we refer to these G values as G_C and G_B , respectively.

For a pair of spectra to exhibit "significant" variability, we require that $G_{\rm B} > 4$ and $G_{\rm C} < 2$. Figure 7 demonstrates the use of these criteria in excluding cases of spurious detections from our sample. These criteria may exclude cases of true BAL variability due to random fluctuations in the continuum regions; however, the use of these criteria allows us to create a conservative sample of spectra showing significant short-timescale BAL variability.

4. Results and Discussion

4.1. BALs Exhibiting Short-timescale Variability

We searched for short-timescale variability in our sample by identifying pairs of epochs with significant variability (as defined above) on rest-frame timescales of less than 10 days. Figure 8 shows all pairs of spectra in which we identified significant short-timescale variability, and Table 5 provides information on which epochs show significant variability and relevant measurements. We identify 54 epoch pairs in 19 unique BALs in 15 different quasars that show significant variability on these short timescales (four quasars had two C IV BALs present that both varied significantly). This indicates that short-timescale BAL variability occurs in at least $55^{+18}_{-14}\%$ of BAL quasars and in $51^{+15}_{-12}\%$ of BAL troughs (upper and lower confidence limits, here and henceforth, are all calculated via Gehrels (1986), unless noted otherwise).

We also examine the frequency of rapid variability among all epoch pairs. In our sample, we have a total of 1460 pairs of sequential epochs separated by less than 10 days in the quasar rest frame. As noted above, 54 of these epoch pairs exhibit significant short-timescale variability, which corresponds to a frequency of $3.7\% \pm 0.5\%$.

The observed high fraction of BAL troughs exhibiting short-timescale variability raises the possibility that all BAL troughs would exhibit short-timescale variability if observed a sufficient number of times. To test this possibility, we consider the following simple model (in which "epoch pairs" refers to subsequent epoch pairs and "variability" to significant short-timescale variability). First, we calculate two probabilities: that an epoch pair will show variability if the immediately previous epoch pair did not show such variability (3.0%) and if the

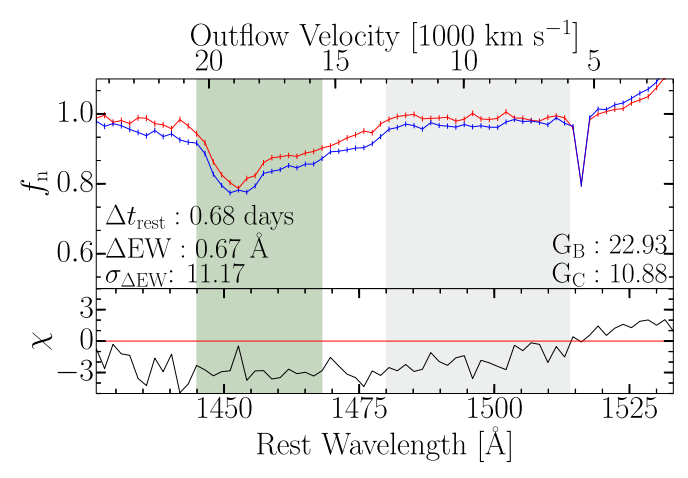


Figure 7. A demonstration of the utility of our additional significance criteria. The spectra shown are from RM 770, MJDs 56715–56717. The top subpanel shows the normalized flux, $f_{\rm n}$. The red line and error bars correspond to the first epoch listed, and blue corresponds to the second epoch. The gray shaded region displays the continuum region used to calculate $G_{\rm C}$. The green shaded region highlights the region containing the BAL being examined—this region was used to calculate $G_{\rm B}$. Relevant measurements ($\Delta t_{\rm rest}$, $\Delta {\rm EW}$, $\sigma_{\Delta {\rm EW}}$, $G_{\rm B}$, and $G_{\rm C}$) are provided. The bottom subpanel shows the χ statistic (showing the difference between the two spectra in units of their uncertainties) as a function of wavelength.

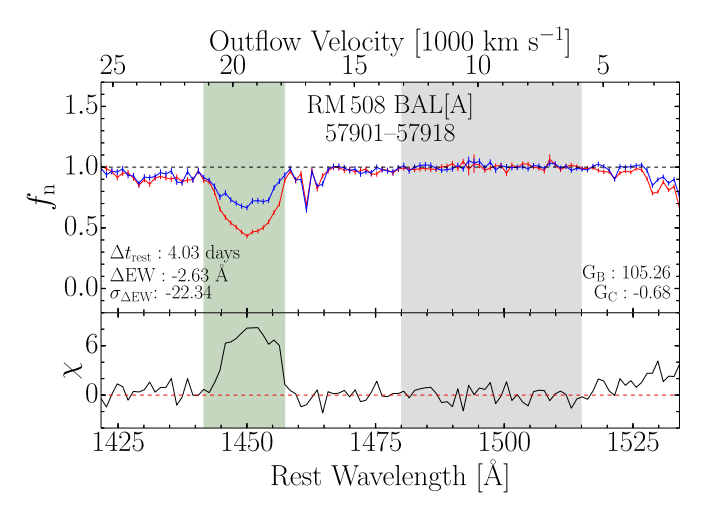


Figure 8. A pair of spectra showing "significant" variability for one epoch pair of RM 508. The top subpanels show the normalized flux, $f_{\rm n}$, with the MJDs of the two epochs provided below the RM identifier in the title of each plot. The red line and error bars correspond to the first epoch listed, and blue corresponds to the second epoch. The gray shaded regions display the continuum regions used to calculate $G_{\rm C}$. The green shaded region highlights the region containing the BAL being examined—this region was used to calculate $G_{\rm B}$. Yellow shaded regions indicate additional C IV BALs, when present. Relevant measurements ($\Delta t_{\rm rest}$, $\Delta {\rm EW}$, $\sigma_{\Delta {\rm EW}}$, $G_{\rm B}$, and $G_{\rm C}$) are provided for each pair of spectra. The bottom subpanels for each pair show the χ statistic (quantifying the difference between the two spectra in units of their uncertainties) as a function of wavelength. Figures for all 54 instances of significant short-timescale variability are provided in the online version of the article.

(The complete figure set (54 images) is available.)

immediately preceding epoch pair did (22%). These probabilities show that significant short-timescale variability is not distributed completely at random in time in a given BAL trough.

We assume the probability of *not* seeing a variability event in a given trough and short-timescale epoch pair is $P_{\text{no}} = 0.97$,

regardless of the exact time separation between subsequent epochs. For a BAL trough observed N_i times, the probability of not seeing a variability event in that BAL is $P_i = 0.97^{(N_i-1)}$. Summing over all troughs in a sample (i = 1 to N_{troughs}), the expected number of BAL troughs without variability events is $N_{\text{no}} = \sum_{i} P_{i}$, with a variance of $\sigma^{2} = N_{\text{troughs}} \bar{P}_{i} (1 - \bar{P}_{i})$, where \bar{P}_i is the average of P_i over all i troughs. This toy model for short-timescale variability occurring in all BAL troughs predicts that we should see 13.5 ± 2.9 troughs without significant variability in our sample of 37 troughs, with an average of 39.5 epoch pairs per trough. This prediction is likely a small underestimate because it ignores cases of three or more epoch pairs in a row showing variability; accounting for that effect would increase $P_{\rm no}$ and $N_{\rm no}$. In reality, we observed 18 such troughs, a $+1.5\sigma$ deviation. Thus, our data are consistent with a toy model in which short-timescale variability occurs in all BAL troughs.

Our observed frequency of rapid variability is significantly higher than that reported by Capellupo et al. (2013); they found that only $12^{+15}_{-7.6}\%$ of their quasar sample (2/17 quasars) showed significant variability on timescales of less than 72 days (they report 29% for a less conservative estimate). As in our study, several of the Capellupo et al. (2013) quasars host multiple BALs—Capellupo et al. (2011) identify 25 unique BALs in the sample of 17 quasars with short-timescale data. Two of these BALs varied on timescales of less than 10 days, corresponding to a BAL variability frequency of $8^{+10}_{-5}\%$ (2/25 BALs). Applying the same arguments above to the Capellupo et al. (2013) sample and assuming $P_{\text{no}} = 0.97$ regardless of exact time separation, we find that their expected number of BAL troughs without observed variability events is $N_{\rm no} = 22.5 \pm$ 1.5. This agrees very well with their true observed number of troughs without variability events, 23. Thus, although our aforementioned frequency of observed short-timescale variability is significantly higher than that of Capellupo et al. (2013), this discrepancy could be explained by their comparative lack of spectral epochs.

We analyzed several properties of the 15 quasars exhibiting significant short-term variability (M_i , z, radio-loudness) and find that none of them is an outlier when compared to the general population of BAL quasars (see Figure 1). None of the varying BAL quasars is radio-loud. Additionally, we investigated whether the BAL troughs that exhibit significant shorttimescale variability are distinct from BAL troughs that do not exhibit such variability in terms of velocity width, mean depth, EW, and centroid velocity $(\Delta v, \langle d \rangle, \text{ EW}, \text{ and } v_{\text{cent}})$. The parameter distributions of the rapidly varying and non-varying BALs were compared using a two-sample Kolmogorov-Smirnov (K-S) test, returning the K-S statistic (D) and the corresponding probability P, which represents the probability that the two samples are drawn from the same parent distribution. We measure D = 0.17 and P = 0.94 for Δv , D = 0.17 and P = 0.94 for $\langle d \rangle$, D = 0.21 and P = 0.80 for EW, and D = 0.22 and P = 0.72 for v_{cent} . Thus, we conclude that varying and non-varying BALs do not fundamentally differ in terms of the aforementioned parameters.

In this sample, we find significant variability on timescales down to 0.57 days, nearly as short as our data probe; the shortest rest-frame timescale probed for each object ranges between 0.1 and 0.3 days, depending on their redshifts. This is the first detection of such short-term variability, to our knowledge, likely because our study intensively explores

Table 5
Short-timescale Variability among Epoch Pairs

Direct timescale variability among Epoch Fairs													
RM ID	BAL ID	MJD ₁ (days)	MJD ₂ (days)	$\Delta t_{ m rest}$ (days)	$\begin{array}{c} \mathrm{EW}_1 \\ (\mathrm{\mathring{A}}) \end{array}$	EW ₂ (Å)	$\Delta \mathrm{EW}$ (Å)	$\sigma_{\Delta { m EW}}$	$G_{ m B}$	G_{C}	$f \\ (\chi > 1)$	$f \\ (\chi < -1)$	
RM 128	A	56768.23	56772.23	1.40	34.9 ± 0.5	31.6 ± 0.5	-3.3 ± 0.8	-4.26	5.15	-0.70	0.32	0.08	620
RM 128	A	56783.25	56795.18	4.16	31.7 ± 0.7	26.4 ± 0.7	-5.3 ± 1.0	-5.08	4.46	0.39	0.32	0.09	610
RM 128	В	56720.45	56722.39	0.68	1.7 ± 0.1	2.6 ± 0.1	0.9 ± 0.2	5.23	8.87	0.29	0.00	0.57	900
RM 128	В	56825.19	56829.21	1.41	2.0 ± 0.1	3.1 ± 0.1	1.1 ± 0.2	5.50	9.41	1.29	0.00	0.86	1500
RM 217	В	56660.21	56683.48	8.27	15.7 ± 0.5	19.2 ± 0.5	3.5 ± 0.7	4.93	4.13	-1.27	0.00	0.41	310
RM 217	В	56683.48	56686.47	1.06	19.2 ± 0.5	16.3 ± 0.5	-2.9 ± 0.7	-4.30	4.33	0.28	0.56	0.15	940
RM 217	В	56686.47	56696.78	3.66	16.3 ± 0.5	19.3 ± 0.4	3.1 ± 0.6	4.76	4.70	-0.77	0.07	0.48	630
RM 257	A	57510.32	57518.31	2.33	40.6 ± 0.4	47.1 ± 0.5	6.4 ± 0.6	10.10	27.03	0.38	0.13	0.54	7250
RM 257	A	57518.31	57543.45	7.32	47.1 ± 0.5	42.1 ± 0.5	-4.9 ± 0.7	-7.11	9.46	1.13	0.49	0.06	3650
RM 257	В	56715.39	56717.33	0.57	4.9 ± 0.1	5.3 ± 0.1	0.4 ± 0.1	4.60	5.26	-0.66	0.00	0.75	510
RM 257	В	56717.33	56720.45	0.91	5.3 ± 0.1	4.9 ± 0.1	-0.4 ± 0.1	-4.64	6.24	-0.42	0.75	0.00	510
RM 257	В	57510.32	57518.31	2.33	4.9 ± 0.1	5.6 ± 0.1	0.7 ± 0.1	5.90	14.09	0.38	0.12	0.62	1010
RM 257	В	57518.31	57543.45	7.32	5.6 ± 0.1	5.1 ± 0.1	-0.6 ± 0.1	-4.32	5.41	1.13	0.62	0.00	760
RM 257	В	57918.16	57933.42	4.44	4.6 ± 0.1	5.3 ± 0.1	0.6 ± 0.1	5.06	7.20	-0.40	0.00	0.75	1010
RM 357	A	56755.34	56768.23	4.10	0.6 ± 0.2	2.1 ± 0.2	1.5 ± 0.3	5.09	5.98	-0.80	0.00	0.80	1140
RM 357	A	56783.25	56795.18	3.79	2.5 ± 0.2	0.6 ± 0.2	-1.9 ± 0.3	-6.08	8.68	1.59	0.90	0.00	2280
RM 357	В	56755.34	56768.23	4.10	11.4 ± 0.3	14.1 ± 0.2	2.6 ± 0.3	8.07	17.98	-0.80	0.11	0.53	2220
RM 357	В	56783.25	56795.18	3.79	15.0 ± 0.2	12.8 ± 0.3	-2.3 ± 0.3	-6.69	10.46	1.59	0.63	0.11	1950
RM 357	В	56804.19	56808.26	1.29	11.6 ± 0.3	13.7 ± 0.2	2.2 ± 0.3	5.88	10.66	0.31	0.05	0.47	1110
RM 357	В	57097.48	57106.47	2.86	4.9 ± 0.4	6.9 ± 0.3	2.0 ± 0.4	4.45	4.21	-0.98	0.00	0.53	550
RM 357	В	57135.17	57159.16	7.63	7.2 ± 0.3	10.4 ± 0.3	3.2 ± 0.4	8.30	16.19	-1.33	0.00	0.68	1380
RM 357	В	57435.40	57451.46	5.11	9.8 ± 0.3	7.0 ± 0.3	-2.8 ± 0.4	-7.10	15.12	0.48	0.68	0.05	1390
RM 357	В	57463.40	57480.60	5.47	6.6 ± 0.3	10.0 ± 0.3 10.0 ± 0.2	-2.8 ± 0.4 3.5 ± 0.4	9.49	19.12	1.89	0.00	0.79	2490
RM 361	A	56813.23	56825.19	4.57	14.5 ± 0.2	16.7 ± 0.2	2.2 ± 0.3	6.29	7.54	1.80	0.00	0.65	2010
RM 508	A	56686.47	56696.78	2.45	6.0 ± 0.0	5.4 ± 0.1	-0.6 ± 0.1	-8.52	16.87	1.72	0.80	0.00	2160
RM 508	A	57185.17	57195.60	2.43	6.7 ± 0.0	6.3 ± 0.1	-0.5 ± 0.1 -0.5 ± 0.1	-6.32 -5.25	4.93	-0.68	0.73	0.07	1300
RM 508	A	57789.44	57805.35	3.78	7.1 ± 0.1	6.2 ± 0.1	-0.3 ± 0.1 -0.8 ± 0.1	-3.23 -9.61	20.33	-0.68 -0.62	0.73	0.07	2380
RM 508				2.84	6.2 ± 0.1	6.6 ± 0.1	-0.8 ± 0.1 0.4 ± 0.1	-9.61 4.29					860
	A	57805.35	57817.32		6.2 ± 0.1 7.1 ± 0.1	6.5 ± 0.1 6.5 ± 0.1	-0.6 ± 0.1	-6.03	4.27	-0.15	0.07	0.53	1730
RM 508	A	57874.21	57892.29	4.30	6.1 ± 0.1	3.5 ± 0.1			4.95	0.45	0.87 0.93	0.00	2810
RM 508	A	57901.21	57918.16	4.03			-2.6 ± 0.1	-22.34	105.26	-0.68		0.00	
RM 508	A	57918.16	57933.42	3.63	3.5 ± 0.1	2.8 ± 0.1	-0.7 ± 0.1	-6.25	9.12	0.08	0.73	0.00	1510
RM 509	В	56780.23	56782.25	0.55	4.4 ± 0.1	5.2 ± 0.1	0.8 ± 0.2	4.88	6.78	0.08	0.00	0.78	710 540
RM 613	A	56686.47	56696.78	3.08	5.0 ± 0.1	5.4 ± 0.1	0.4 ± 0.1	4.26	4.57	0.15	0.00	0.44	810
RM 613	A	56751.34	56755.34	1.19	5.1 ± 0.1	4.6 ± 0.1	-0.5 ± 0.1	-4.96	5.13	1.24	0.56	0.00	
RM 613	A	56772.23	56780.23	2.39	4.7 ± 0.1	4.1 ± 0.1	-0.6 ± 0.1	-7.28	8.76	1.00	0.88	0.00	1630
RM 631	A	56783.25	56795.18	3.21	6.5 ± 0.1	7.2 ± 0.1	0.7 ± 0.2	4.37	6.73	1.28	0.15	0.46	470
RM 717	A	56715.39	56717.33	0.61	17.3 ± 0.5	23.6 ± 0.7	6.2 ± 0.9	7.14	6.65	1.07	0.02	0.50	1690
RM 717	A	56717.33	56720.45	0.98	23.6 ± 0.7	17.7 ± 0.6	-5.8 ± 0.9	-6.44	5.17	1.84	0.56	0.06	1690
RM 722	A	57185.17	57195.60	2.94	10.5 ± 0.1	8.9 ± 0.2	-1.5 ± 0.2	-7.28	11.79	1.34	0.82	0.06	740
RM 730	A	56751.34	56755.34	1.08	24.5 ± 0.1	23.5 ± 0.1	-0.9 ± 0.2	-5.08	5.17	-0.56	0.41	0.06	750
RM 730	A	56755.34	56768.23	3.49	23.5 ± 0.1	24.6 ± 0.1	1.1 ± 0.2	6.11	4.20	0.41	0.04	0.49	1250
RM 743	A	56715.39	56717.33	0.71	9.3 ± 0.5	12.7 ± 0.6	3.4 ± 0.7	4.52	4.92	0.54	0.10	0.43	320
RM 743	A	56780.23	56782.25	0.74	12.7 ± 0.4	10.0 ± 0.4	-2.6 ± 0.6	-4.69	7.45	0.16	0.52	0.10	1610
RM 770	A	56825.19	56829.21	1.41	3.2 ± 0.0	3.5 ± 0.0	0.3 ± 0.1	5.54	4.72	0.67	0.00	0.73	1580
RM 786	A	56683.48	56686.47	0.98	2.2 ± 0.1	1.6 ± 0.1	-0.6 ± 0.1	-5.03	6.42	1.56	0.67	0.00	590
RM 786	В	56660.21	56664.51	1.42	31.9 ± 0.1	33.6 ± 0.2	1.8 ± 0.2	7.89	12.27	1.21	0.03	0.74	2290
RM 786	В	56669.50	56683.48	4.60	34.3 ± 0.3	32.2 ± 0.1	-2.1 ± 0.3	-6.35	7.92	1.22	0.61	0.03	2590

Hemler et al.

Table 5 (Continued)

RM ID	BAL ID	MJD ₁ (days)	MJD ₂ (days)	$\Delta t_{\rm rest}$ (days)	EW ₁ (Å)	EW ₂ (Å)	ΔEW (Å)	$\sigma_{\Delta ext{EW}}$	$G_{ m B}$	$G_{ m C}$	$f \\ (\chi > 1)$	$f \\ (\chi < -1)$	$\Delta v_{\rm co}^{}$
RM 786	В	56683.48	56686.47	0.98	32.2 ± 0.1	31.4 ± 0.1	-0.8 ± 0.2	-4.92	4.48	1.56	0.45	0.06	290
RM 786	В	56686.47	56696.78	3.39	31.4 ± 0.1	32.8 ± 0.1	1.4 ± 0.2	9.17	13.20	0.38	0.00	0.71	3140
RM 786	В	56717.33	56720.45	1.02	33.3 ± 0.1	32.6 ± 0.1	-0.7 ± 0.2	-4.58	4.99	0.84	0.52	0.10	1430
RM 786	В	56745.28	56747.42	0.70	32.0 ± 0.1	33.3 ± 0.1	1.3 ± 0.1	8.73	15.19	-0.49	0.00	0.74	2290
RM 786	В	56749.37	56751.34	0.65	33.7 ± 0.1	32.1 ± 0.1	-1.5 ± 0.2	-9.39	18.63	-0.89	0.77	0.03	3970
RM 786	В	56772.23	56780.23	2.63	32.8 ± 0.1	33.5 ± 0.1	0.7 ± 0.1	5.66	7.68	-0.41	0.06	0.58	1140
RM 786	В	56804.19	56808.26	1.34	32.6 ± 0.1	33.7 ± 0.1	1.2 ± 0.2	6.48	7.88	1.53	0.03	0.48	1710

Note.

(This table is available in machine-readable form.)

 $^{^{\}rm a}$ Coordinated velocity (see Section 4.3.1), in units of km s $^{\rm -1}$.

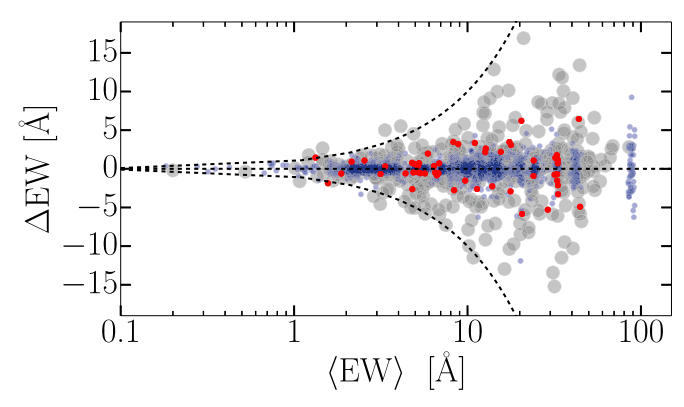


Figure 9. Sequential epoch ΔEW vs. average EW for all pairs of spectra in our sample (blue dots) and our rapidly varying pairs (red dots). Gray dots represent data from Filiz Ak et al. (2013), Barlow (1993), Lundgren et al. (2007), and Gibson et al. (2008). The horizontal dashed line shows $\Delta EW=0$ and the curved dashed lines show $\langle EW\rangle=\Delta EW$. Our sample shows the same general distribution as previous work.

timescales much shorter than previous works (see Table 1). BAL variability has thus far been observed on all timescales that have been examined.

An assortment of variability amplitudes appear in our rapidly varying pairs of spectra; however, in most cases, the fractional change in EW is fairly small. This is as expected, because previous studies have established that longer timescales correspond to larger fractional changes in EW (e.g., Filiz Ak et al. 2013). We do not observe BAL variations to be preferentially strengthening or weakening on these short timescales—specifically, 26 out of 54 epoch pairs show a decrease in EW, while the remainder exhibit an increase. In some cases, however, rather dramatic variability occurs. For example, between MJDs 57901 – 57918, BAL[A] in RM 508 underwent a very significant (Δ EW > 20σ) EW change. The EW of the BAL dropped from 6.12 Å to 3.49 Å (a factor of 1.8) within a time span of about four days in the quasar rest frame (see Figure 8).

Another example of dramatic variability occurs in RM 357, which has a high-velocity BAL (denoted BAL[A] in our tables and figures) that is present at the beginning of the campaign. This BAL disappears and reappears at various points during the campaign. The EW in the absorption region containing BAL [A] steadily weakens during the first few months of the campaign (see Figure 5), and decreases to within 3σ of zero by MJD 56755 (at this point it is no longer formally considered a BAL). The absorption feature then reappeared as a formal BAL between MJD 56755 and 56768 ($\Delta t_{\text{rest}} = 4.1$ days), and formally disappeared again between MJD 56783 and 56795 $(\Delta t_{\rm rest} = 3.79 \text{ days})$. Both of these epoch pairs are indicated in Figure 5 by red coloring. For each epoch where the BAL is not present (MJDs 56755 and 56795), we searched for residual low-level absorption. We consider both of these epochs to be "pristine" cases of BAL disappearance (see, e.g., Filiz Ak et al. (2012) or De Cicco et al. (2018) for further examples of "pristine" BAL disappearance) because the flux at all pixels within the trough region deviates by less than 3σ from the continuum.

4.2. Variability Characteristics of the Entire Quasar Sample

We now compare the distributions of some variability parameters within our sample to those from previous studies.

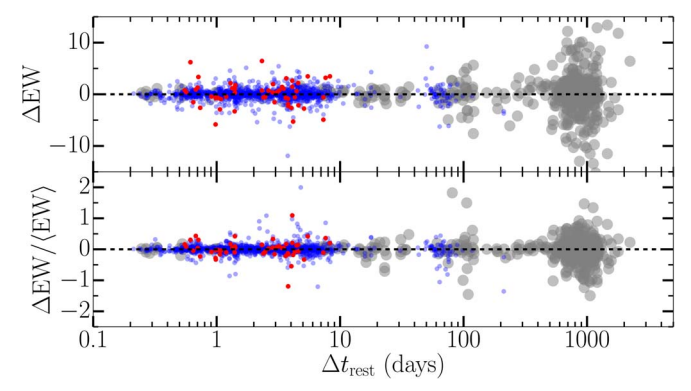


Figure 10. ΔEW and $\Delta EW/\langle EW \rangle$ vs. rest-frame time difference for every sequential epoch pair of every object (blue dots) and for our pairs of epochs that are identified as rapidly varying (red dots). Gray circles indicate data from Filiz Ak et al. (2013), Barlow (1993), Lundgren et al. (2007), and Gibson et al. (2008). Our sample shows the same general distribution as previous work.

Figure 6 shows the distribution of ΔEW from every sequential epoch pair in our sample compared to previous work, Figure 9 displays ΔEW as a function of $\langle EW \rangle$, and Figure 10 shows the distribution of ΔEW and $\Delta EW/\langle EW \rangle$ as functions of Δt_{rest} . Two BALs (RM 217 BAL[A] and RM 357 BAL[A]) disappeared at least once over the course of the campaign; in cases where these BALs were absent in both epochs, fluctuations in EW are dominated by noise. Thus, for our sample investigations (Figures 9 and 10), we exclude epoch pairs where both of the EW values are consistent with zero to within 3σ .

Together, Figures 6, 9, and 10 reveal that the ΔEW distributions of our sample contain no significant outliers in comparison with the distributions of other samples. While Figure 10 appears to show excessive variability at short timescales, Figure 6 demonstrates that such variability represents the rare tails of the ΔEW distribution and that the majority of our measurements are, as expected, small-amplitude variations.

4.3. Causes of Variability

There are many different models of the processes that drive BAL variability. Previous studies have found that, in some cases, the variability is consistent with models involving changes in the amount of ionizing radiation received by the gas (e.g., Misawa et al. 2010; Filiz Ak et al. 2012, 2013; Capellupo et al. 2012; Grier et al. 2015; Wang et al. 2015; He et al. 2017). Other studies of BAL variability suggest that the variability is due to the transverse movement of outflow material across the line of sight of the observer (often referred to as "cloudcrossing," e.g., Lundgren et al. (2007), Gibson et al. (2008), Hall et al. (2011), Vivek et al. (2012), and Capellupo et al. (2013)). Changes in ionizing flux can be difficult or impossible to observe, as ion species like C IV are ionized by radiation in the extreme ultraviolet, which has been reported to be more variable than the optical or near-ultraviolet (e.g., Marshall et al. 1997). Thus, the variability in the ionizing continuum may not be reflected by observations of optical or near-ultraviolet continuum variability (see Section 4.2.1 of Grier et al. (2015) for a more detailed discussion).

It is thus advantageous to use other evidence, such as certain characteristics of the variability or other properties of the quasar spectra, to identify the most likely cause of variability. For example, the presence of coordinated variability across the full profile of a BAL trough and between distant C IV troughs

provides evidence in support of variability driven by changes in the ionization state of the outflow gas. The presence of BAL troughs of other species can provide information on whether the C IV BAL is highly saturated (e.g., Capellupo et al. 2017); a single- τ saturated BAL trough will not change its EW in response to changes in ionizing continuum in the same manner as unsaturated troughs. Thus, observed variability in saturated BALs would favor cloud-crossing models. Below, we examine several characteristics of the observed short-timescale BAL variability and the corresponding quasar spectra in order to determine the physical models responsible.

4.3.1. Coordinated Variability across the Width of Individual BAL Troughs

We first search for coordinated variability across individual BAL troughs. At each (binned) pixel in a normalized trough, we calculate χ , the error-normalized difference in flux between the two spectra. We assume that all pixels with measured $|\chi| < 1$ exhibit only noise-dominated fluctuations consistent with zero variability. For each rapidly varying BAL, we measure the fraction of pixels in the BAL trough with $\chi > 1$, denoted $f(\chi > 1)$, and the fraction with $f(\chi < -1)$. The various possible combinations of these parameters can be interpreted as follows:

- 1. High values of either $f(\chi > 1)$ or $f(\chi < -1)$ correspond to variability consistent with being coordinated in the same direction across a trough. Such variability is consistent with a model in which ionization-state changes drive the observed BAL variations. These cases cannot be explained solely by crossing clouds because such clouds are unlikely to cause coordinated variability over thousands of km s⁻¹ on timescales of days or less. There may be some cases where part(s) of the trough vary in the same direction, but unequally (e.g., RM128 BAL[A] MJDs 56768–56772; see Figure Set 8). Such variability may be explained by ionization-state changes with a range of densities across the outflow (see Arav et al. 2012, Appendix A), or with ionization-state variability and crossing clouds.
- 2. If χ is nonzero in parts of the trough and effectively zero in other parts, we are seeing variable and stable regions of the trough, respectively (e.g., RM 357 BAL[B] MJDs 56755–56768, RM 717 BAL[A] MJDs 56717–56720, or RM 786 BAL[B] MJDs 56745–56747). Such variability may be consistent with crossing clouds if the velocity widths of the variable regions are sufficiently small, but this behavior can also be explained by ionization variability combined with saturation or different densities within the outflow.
- 3. If $f(\chi > 1)$ and $f(\chi < -1)$ are both significantly nonzero, we are seeing variability in both directions simultaneously (i.e., the BAL is weakening in some regions and strengthening in some regions). Such variability may be consistent with crossing clouds or ionization variability if the density is nonuniform within the outflow.

Figure 11 shows $f(\chi > 1)$ versus $f(\chi < -1)$ for our rapidly varying pairs of spectra, and we provide $f(\chi > 1)$ and $f(\chi < -1)$ values in Table 5. BALs experiencing coordinated variability across the trough (the first situation described above) cluster along either the horizontal or vertical axis of Figure 11.

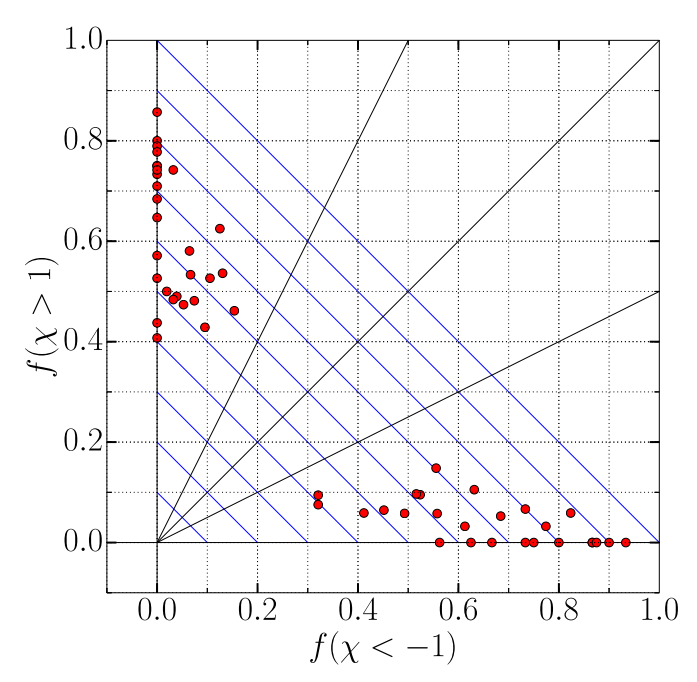


Figure 11. The fraction of pixels with $\chi > 1$ ($f(\chi > 1)$) as a function of the fraction of pixels with $\chi < -1$ ($f(\chi < -1)$) for the epoch pairs showing rapid BAL variability (red circles). Black solid lines indicate ratios of 2:1, 1:1, and 1:2 to guide the eye, and the blue diagonals represent lines of constant $f(-1 < \chi < 1)$.

Cases showing coordinated variability in the same direction across the majority of the trough (e.g., RM 508) appear farthest from the origin, and objects for which only part of the trough varies lie closer to the origin along the axes. BALs with significant variability in both directions (the third scenario described above) will lie close to a 45° line. All of our cases lie on or between the vertical or horizontal axes and the lines indicating a 2:1 ratio between the two measured quantities. Most of the sets of measurements are consistent with situations (1) and (2) above, which suggests that ionization variability likely plays a role.

We see no cases representing the scenario (3) described above, where there are significant amounts of variability in both directions (i.e., part of the trough strengthens while another part weakens). However, we note that our aforementioned variability significance criteria select against such cases. Consider, for example, a scenario in which half of a BAL strengthens by some large amount, and the other half weakens by a similar amount. The ΔEW of such a case would approach zero. Thus, this case would not be flagged as significant by our $\sigma_{\Delta EW} > 4$ criterion, although significant variability could exist in the individual regions within the BAL. Such preferential selection could help explain the lack of variability in both directions in our sample (see Figure 11). However, we searched our data for potential cases of variability in opposite directions and find no clear examples of this behavior in our sample.

We also measured the largest number of contiguous pixels in each trough with $\chi > 1$ and $\chi < -1$ and denote this quantity as $\Delta \nu_{\rm co}$ —this value is the largest velocity width with "coordinated" variability-state changes. These numbers are provided in Table 5 for each pair of epochs. There is a large variety of $\Delta \nu_{\rm co}$ within our sample, ranging from just under $300\,{\rm km\,s^{-1}}$ to just under $4000\,{\rm km\,s^{-1}}$, indicating a wide variety of coordinated velocity widths. More than half of epoch pairs

show coordinated variability in regions >1000 km s⁻¹. Large regions of coordinated variability can be explained by ionization variability, but models that rely on cloud-crossing scenarios must be able to explain coordinated variability across such velocity widths, e.g., through time-dependent studies of accretion-disk winds (Proga et al. 2012).

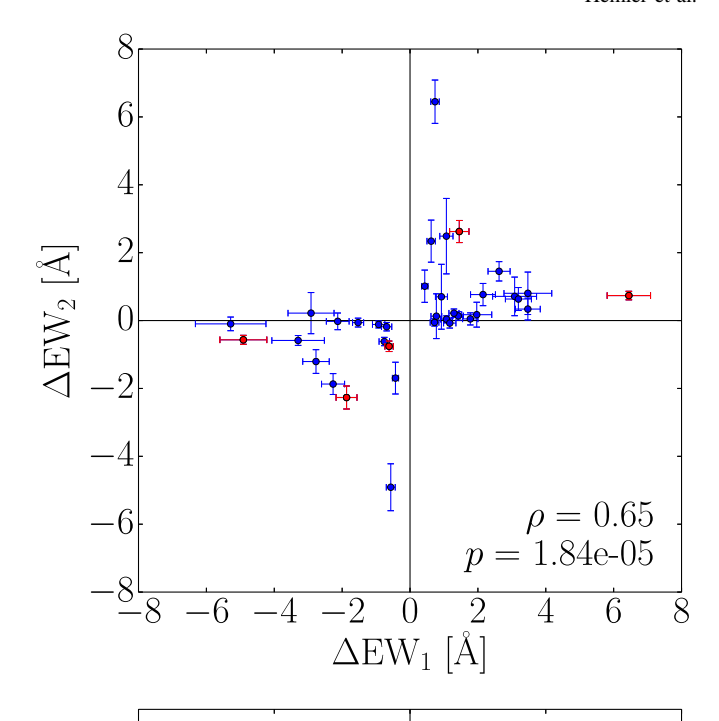
4.3.2. Coordinated Variability between Additional C IV BALs

Seven of our 15 quasars hosting rapidly varying BALs (RM 128, 217, 257, 357, 509, 730, and 786) have additional C IV BALs present in their spectra at different velocities. These quasars provide an opportunity to search for coordination between rapidly varying C IV troughs and those at different velocities—such coordination was reported by Capellupo et al. (2012), Filiz Ak et al. (2012, 2013), and De Cicco et al. (2018) on longer time baselines. For all pairs of epochs where at least one of the BALs experienced significant rapid variations, we also explore the behavior of the other BAL during that same time period. Figure 12 shows Δ EW for each pair of significantly varying C IV BALs. In addition, the behavior of the additional C IV BALs can be compared to the rapidly varying BALs using Figure Sets 5 and 8.

We have 36 pairs of spectra with at least one BAL identified as rapidly varying in quasars hosting a second BAL. A detailed discussion of each individual object and its additional C IV BAL is provided in the Appendix. Figure 12 shows a potential correlation between ΔEW of C IV BAL pairs, providing tentative evidence for coordinated variability between the two troughs in many cases. We also performed a Spearman rank correlation test to determine the strength of the correlation between the two quantities, computing the Spearman rank-order correlation coefficient ρ and the corresponding probability p that describes the likelihood of obtaining the measured ρ value if the two quantities are actually uncorrelated. We obtain $\rho = 0.65$ and $p = 1.84 \times 10^{-5}$ for ΔEW changes and $\rho = 0.4$ and $p = 1.44 \times 10^{-2}$ for $\Delta EW/\langle EW \rangle$, indicating that the EW changes of the two C IV troughs are correlated. We interpret this as evidence for coordinated variability between C IV BAL troughs in our sample.

4.3.3. Si IV and Al III

The presence of BALs at velocities corresponding to the C IV BAL but arising from other absorption species can provide clues to the physical properties of BAL outflows (e.g., Filiz Ak et al. 2014; Capellupo et al. 2017). To investigate this, Filiz Ak et al. (2014) divided their sample of C IV BALs into categories according to the presence of other species: If neither Si IV $\lambda\lambda$ 1393,1403 nor Al III $\lambda\lambda$ 1855,1863 is present at velocities corresponding to an identified C IV BAL, said BAL is denoted a C IV₀₀ trough. If a Si IV BAL is present but Al III is not detected, it is denoted as a C IV_{S0} trough, ¹² and if both Si IV and Al III BALs are present at corresponding velocities, it is denoted as a C IV_{SA} trough. In a sample of 851 BAL troughs, they find that $13\% \pm 1\%$ of their BAL troughs fall into the C IV₀₀ category, $61\% \pm 3\%$ into the C IV_{s0} or $\text{C\,{\sc iv}}_{s0}$ categories, and 26% \pm 1% into the $\text{C\,{\sc iv}}_{SA},\,\text{C\,{\sc iv}}_{Sa},\,\text{or}$ C IV_{sa} categories.



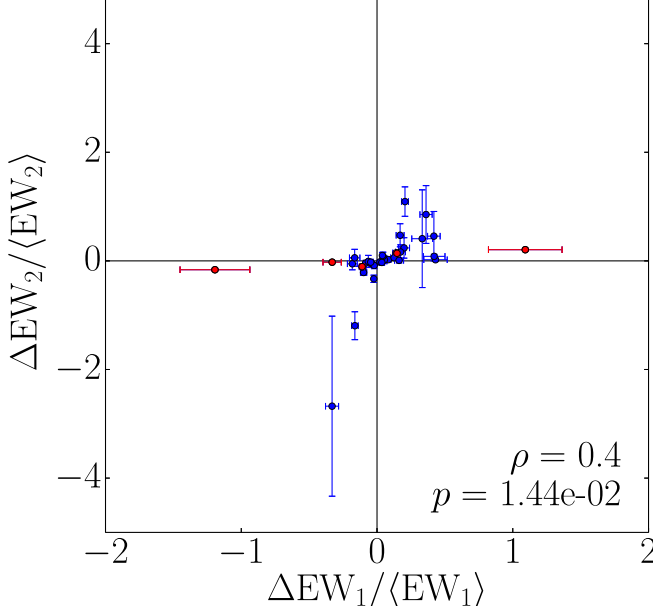


Figure 12. ΔEW (top panel) and $\Delta EW/\langle EW \rangle$ (bottom panel) of accompanying C IV BALs as a function of the ΔEW of the rapidly varying BALs. In all cases, ΔEW_1 refers to the measurement of the BAL that is identified as rapidly variable, and ΔEW_2 refers to the accompanying BAL during the same pair of epochs. Blue points represent pairs where only one of the BALs (ΔEW_1) passed our criteria for rapid variability; in these cases, the second BAL varied with a lower significance (or is sometimes statistically consistent with zero variability). Red points represent pairs of epochs where both BALs varied significantly. The results of a Pearson correlation test are provided in the lower-right corner of each subplot; ρ is the measured Pearson coefficient and ρ is the corresponding probability that the measured ρ would be obtained randomly if the two quantities were actually uncorrelated.

We visually inspected the mean spectra of our quasars to determine whether or not these additional species are present in our sample, and assigned each BAL a category following Filiz Ak et al. (2014), with one notable change: we do not differentiate between BALs and mini-BALs when considering Si IV and Al III. We thus place our BAL troughs into only three

 $^{^{12}}$ The troughs are designated C IV $_{s0}$ if Si IV is a mini-BAL rather than a formal BAL, C IV $_{sa}$ if Si IV and Al III are both present as mini-BALs, and C IV $_{sa}$ if the Si IV feature is a formal BAL but the Al III feature is a mini-BAL.

categories (C $\rm IV_{00}$, C $\rm IV_{S0}$, and C $\rm IV_{SA}$) as long as a BAL or mini-BAL of the other species is present. In some cases, there was evidence for absorption of Si IV or Al III that was not deep enough to meet the normalized flux threshold of 0.9 used in BAL searches, and thus the absorption is considered undetected. Our classifications for all identified BALs are given in Table 3, with details on individual objects given in the Appendix. There are three cases in our BAL trough sample where there is not sufficient coverage of the Si IV region to determine a class—we denote these as C $\rm IV_{N0}$ troughs in Table 3.

In our sample of 34 troughs with coverage of the Si IV region, we find 15 C IV₀₀ troughs $(44^{+15}_{-11}\%)$ of our sample), 13 C IV_{S0} troughs $(38^{+14}_{-11}\%)$, and six C IV_{SA} troughs $(18^{+11}_{-7}\%)$. This is a substantially higher fraction of C IV₀₀ BALs than is present in the Filiz Ak et al. (2014) sample. This is primarily due to the different velocity ranges used in our BAL searches—Filiz Ak et al. (2014) search only outflow velocities ranging from 3000 to $20,000 \, \mathrm{km \, s^{-1}}$ in their work, while we extend ours from an apparent inflow velocity of 1000 km s⁻¹ to an apparent outflow velocity of 30,000 km s⁻¹. Many of our BALs, primarily C_{IV}₀₀ troughs, extend into the ranges excluded by Filiz Ak et al. (2014) and would be excluded if we imposed similar velocity restrictions—imposing these restrictions results in much better consistency between the observed percentages of each category. Another likely contributor to the different percentages of each kind of trough is that we are using coadded spectra to search for BALssometimes including more than 60 spectra, whereas Filiz Ak et al. (2014) used only single-epoch spectra. Our mean spectra are thus generally much higher-SN, which allows us to detect weaker BAL troughs (which are often missed due to noise). Because C IV₀₀ troughs are generally weaker than BALs in the other two categories (Filiz Ak et al. 2014), we expect that the use of coadded/mean spectra also contributes to the higher incidence of C IV₀₀ troughs in our sample.

Among only our 19 rapidly varying BAL troughs, we observe a distribution that is consistent with our full sample: nine $(50^{+23}_{-16}\%)$ of the 18 BALs with short-term variability and Si IV coverage fall into the C IV₀₀ category, six $(33^{+20}_{-13}\%)$ fall into the C IV_{S0} category, and three $(17^{+16}_{-9}\%)$ fall into the C IV_{SA} category (the remaining rapidly varying BAL, RM 361 BAL [A], does not have wavelength coverage of the Si IV region).

When a deep Si IV trough accompanies the observed C IV trough, the C IV trough is likely to be heavily saturated, given the relative cosmic abundances of Si and C and the relative ionic abundances expected in BAL outflows (e.g., Figure 4 of Hamann et al. 2000). Half of our rapidly varying BAL troughs show accompanying Si IV, which indicates saturation and suggests that cloud-crossing may play a part in the observed variability in many of our BALs, as saturated troughs will not respond to changes in the incident ionizing flux in the same manner as unsaturated troughs. However, the presence of saturated C IV troughs is not necessarily solid evidence for simple cloud-crossing scenarios.

For example, consider RM 257 BAL [A], a C IV_{SA} trough with two pairs of epochs identified as rapidly variable. The BAL shows coordinated variability across velocities of $\sim 3600 \, \mathrm{km \, s^{-1}}$ and $\sim 7250 \, \mathrm{km \, s^{-1}}$ (about 20% and 40% of the entire trough width). This coordinated variability is suggestive of ionization-state changes as the driving mechanism. In addition, this quasar also

contains a second, lower-velocity BAL that varies significantly in the same direction (also naturally explained by ionization-state changes). However, the presence of Si IV and Al III BALs indicates that the C IV BAL is likely highly saturated; as discussed above, variability in saturated troughs is more easily explained by cloud-crossing scenarios. At face value, the evidence presented by this BAL seems contradictory.

However, coordinated variability over such a wide velocity range can be explained by a model including inhomogeneous partial covering of some type; that is, different parts of the quasar emission regions are covered by absorbers of different optical depths along our sight line (e.g., de Kool et al. 2002; Arav et al. 2005; Sabra & Hamann 2005). For example, the optical depth values might follow a power-law distribution (e.g., Aray et al. 2008), with a large fraction of the emitting area covered by gas optically thick in C IV and a small fraction covered by optically thin gas. Variations in the ionizing continuum leading to variations in the optical depth values would yield a more detectable change in residual flux from the emitting area covered by optically thin gas than from the emitting area covered by optically thick gas. A BAL outflow exhibiting inhomogeneous partial covering therefore can exhibit strong Si IV and even P V absorption in a trough that nonetheless exhibits variability in the CIVEW that is caused by ionization-state changes. Simultaneously modeling the variability of CIV and Si IV in such cases may constrain inhomogeneous partial covering models; however, we defer such detailed analysis to a future work.

4.3.4. PV

We also searched for $PV\lambda\lambda 1112,1118$ absorption in our significant-variability sample. PV is a lower-abundance ion that has an ionization energy similar to that of CIV, and its presence, like that of Si IV, indicates that the corresponding component of C IV absorption is highly saturated (e.g., Capellupo et al. 2017). There have been differing reports on the frequency of P V BALs; Capellupo et al. (2017) report that only 3-6% of BAL quasars examined show detectable PV, while Filiz Ak et al. (2014) estimate that about half of their sample contains visible signs of PV absorption. The incidence of detectable PV rises when other species, such as Si IV or Al III, are present—Filiz Ak et al. (2014) report that 88% of their CIVSA troughs show detectable PV, about half of the C IV_{S0} troughs show detectable P V, and only 12% of C IV₀₀ troughs are accompanied by PV absorption. The discrepancy in the PV detection percentages between Capellupo et al. (2017) and Filiz Ak et al. (2014) is likely due to differing identification criteria: Capellupo et al. (2013) note that they are extremely conservative in identifying PV and that their algorithm is biased against weaker and narrower features, whereas Filiz Ak et al. (2014) use visual inspection to identify PV, and may thus identify many features that are excluded by the strict criteria used in the former work.

In the cases in which the PV region is covered by our spectra, it falls toward the very blue end of the spectrum, which often contains significant noise, causing difficulties in its reliable detection, and this difficulty is compounded by the fact that it falls within the $Ly\alpha$ forest. A detailed analysis is thus beyond the scope of this work—however, we visually inspected the spectra for signs of broad PV absorption that corresponds to the velocities of our 37 identified CIV BALs. The results for each identified BAL in our sample are presented

in Table 3. Only 15 of our 37 BALs have coverage of the PV region at corresponding velocities; for these 15 C IV BALs, we find tentative signs of accompanying PV in six cases $(40^{+23}_{-15}\%)$.

Three of the six likely P v BALs accompany rapidly varying C IV BALs—in quasars RM 257, RM 631, and RM 730. All three also contain Si IV absorption (RM 631 and RM 730 are both C IV $_{\rm S0}$ troughs and RM 257 BAL[A] is a C IV $_{\rm SA}$ trough), further supporting saturation. One would thus expect that the observed variability in these BALs is most likely due to cloud-crossing or, as discussed above (Section 4.3.3), by inhomogeneous partial covering scenarios.

4.4. Physical Constraints from Ionization Variability

The evidence presented above suggests that the variability we observe is due to a variety of causes; in some cases (e.g., RM 508), we find substantial evidence in support of the ionization-change scenario, while in others (e.g., RM 730; see Section 4.3.4), the evidence may point to to cloud-crossing as the more likely scenario. We here carry out one example calculation of some of the physical constraints that can be obtained in the case of ionization changes for one such BAL. To do so, we adopt a model for ionization variability in optically thin C IV gas (details are provided in the Appendix). This model is only plausible for BAL troughs with a C IV₀₀ designation in Table 3, indicating that neither Si IV nor Al III accompany the C IV absorption; we do not expect ionization variability in optically thin C IV gas to explain variability in troughs with CIVSA or CIVSO designations, though ionization variability may play a role if the optical depth is inhomogeneous (see Section 4.3.3).

We choose our most significant case, RM 508, as our case study. BAL[A] in this quasar shows variability at a significance of $>20\sigma$ over a period of just four days in the quasar rest frame (see Figure 8). Following the procedure outlined in the Appendix, we find that the observed variability in RM 508 is consistent with a model of an absorber that fully covers the continuum source, is optically thin in C IV (with a maximum optical depth $\tau_{\rm max} = 0.847 \pm 0.024$), has constant electron density over its velocity range, and responds to a variable ionizing flux by a drop in optical depth of a factor of $\bar{B} = 2.04 \pm 0.07$ in 4.03 rest-frame days. Of course, consistency with a model is not proof the model is correct, but it is encouraging that simple absorber models may be useful in constraining the physical parameters of absorbers and of quasar ionizing flux variability (though we leave the latter as a topic for future work).

Our observations can further be employed to constrain the density and radial distance of quasar outflows (e.g., Grier et al. 2015). For ionization state i of some element, outflow density can be constrained given the EWs of two epochs (EW₁ and EW₂), the rest-frame time difference between these epochs ($\Delta t_{\rm rest}$), the ion's recombination coefficient to ionization state i-1 (α_{i-1}), and several simplifying assumptions (Arav et al. 2012; Rogerson et al. 2015). The relationship between these variables and the density constraint is

$$n_e > \log(\text{EW}_1/\text{EW}_2)/\alpha_{i-1}\Delta t_{\text{rest}}.$$
 (4)

A derivation of Equation (4) is given in Appendix B.2. We assume an outflow temperature approximately equal to that of C IV-region broad line region gas, $\log T = 4.3$ (e.g., Krolik 1999). For this temperature, the C III recombination coefficient

quoted by the CHIANTI online database is $\alpha_{\rm CIII} = 2.45 \times 10^{-11} \, {\rm cm}^3 \, {\rm s}^{-1}$ (Dere et al. 1997; Landi et al. 2013). We utilize this recombination coefficient for subsequent calculations.

With Equation (4), we treat two cases of short-timescale variability to constrain density: the most significantly varying epoch pair (RM 508 BAL[A], MJDs 57901–57918, $\sigma_{\Delta EW} =$ -22.34) and the most rapidly varying epoch pair of a CIV₀₀ BAL exhibiting decreasing EW (RM 257 BAL[B], MJDs 56717–56720, $\Delta t_{\rm rest} = 0.91$ days). These epoch pairs return density constraints of $n_e \gtrsim 6.5 \times 10^4 \, {\rm cm}^{-3}$ and $n_e \gtrsim 4.1 \times 10^{-3} \, {\rm cm}^{-3}$ 10⁴ cm⁻³, respectively. Using data on RM 613 from Grier et al. (2015) in Equation (4), we calculate a density constraint of $n_e \gtrsim 3.4 \times 10^4 \, \mathrm{cm}^{-3}$. Thus, the conservative approach we adopt in Equation (4) yields a lower-limit density from the largeamplitude variability in RM 508 BAL[A] that is about a factor of two larger than those from RM 257 BAL[B] in this work or from RM 613 reported by Grier et al. (2015). Previous studies (e.g., Arav et al. 2013; Borguet et al. 2013) have reported density constraints on the order of $n_e > 10^3 - 10^4 \,\mathrm{cm}^{-3}$ for outflows at radii of kiloparsec scales—our measured densities are consistent with such measurements.

The radial distance from the quasar to the outflow for which the previously calculated density constraint remains valid can also be constrained via

$$r > \sqrt{\int_{\nu_i}^{\infty} \frac{(L_{\nu}/h\nu)\sigma_{\nu}}{4\pi n_e \alpha_{i-1}} d\nu}$$
 (5)

where σ_{ν} is the cross section of photons with energy $h\nu$ and ν_i is the ionization energy of ionization species (i-1). A derivation of Equation (5) is given in Appendix B.3. Note that both the density and radius constraints are conditional; either the gas is more distant and has a greater n_e than the respective lower limits above, or it is located closer than the radius limit with no constraint on its density (see Figure 14 of Rogerson et al. 2015).

We determined $L_{\rm Bol}$ of RM 257 and RM 508 using their respective observed flux densities at 3000 Å 1350 Å and adopting bolometric correction factors of 5 and 4, respectively (bolometric corrections factors are from Richards et al. 2006). We calculate $L_{\rm Bol} = 7.64 \times 10^{46}\,{\rm erg\,s^{-1}}$ for RM 257 and $L_{\rm Bol} = 3.32 \times 10^{47}\,{\rm erg\,s^{-1}}$ for RM 508. Adopting the UV-soft spectral energy distribution of Dunn et al. (2010), we calculate L_{ν} and integrate Equation (5), returning radial distance constraints of $r \gtrsim 248\,{\rm pc}$ and $r \gtrsim 405\,{\rm pc}$ for RMs 257 and 508, respectively. Additionally, we rescale the RM 613 radial distance constraint $r \gtrsim 120\,{\rm pc}$ reported by Grier et al. (2015) to the improved density constraint calculated via Equation (4), yielding a constraint of $r \gtrsim 406\,{\rm pc}$. Our conditional distance constraints for all three quasars for which we have done the calculations (RM 257, RM 508, and RM 613) are thus all on the order of hundreds of parsecs.

Such large radii are inconsistent with the $\sim 10^{-3}$ pc launching radius distance suggested by previous theoretical studies (e.g., Murray et al. 1995; Proga 2000; Higginbottom et al. 2013). However, various studies have reported BAL outflows at greater distances (e.g., see Table 10 of Dunn et al. (2010), with more recent works including, e.g., Xu et al. (2018)), and Arav et al. (2018) report evidence that more than half of all BALs are found at distances of greater than 100 pc. Our conditional distance constraints are consistent with this

claim—although, because they are conditional, they should not be viewed as direct support for it.

5. Summary and Future Work

We have systematically searched for short-timescale (<10 day) variability in a sample of 37 distinct C IV BALs in 27 unique quasars using data from the SDSS-RM project, which contains a large number of spectral epochs at a high cadence compared to previous studies of BAL variability. We further examine these spectra to evaluate models for variability mechanisms and compare our observed variability to previous sample-based studies (e.g., Filiz Ak et al. 2013). Our main findings are the following:

- 1. We have discovered 54 cases of significant rapid variability in 19 unique BALs (see Section 4.1) in 15 out of the 27 quasars in our sample (55⁺¹⁸₋₁₄%), 19 of 37 C IV BAL troughs (51⁺¹⁵₋₁₂%), and 54 of 1460 epoch pairs (3.7% ± 0.5%). This variability is on rest-frame timescales of 0.55–8.27 days, with a median of 2.55 days. This result demonstrates that short-term BAL variability is common; it has not been observed frequently in the past, likely because high-SN observations intensively probing these short timescales did not exist. These quasars and their BAL troughs do not appear to be distinctive; their properties are similar to those of the general quasar population. See Section 4.1.
- 2. We compare the overall variability properties of our sample (ΔEW and fractional ΔEW) to previous studies to determine whether our rapid variability is unusual or more extreme than previously reported. The amplitude of variability in our sample does not appear to differ qualitatively from that previously observed on comparable or slightly longer timescales (see Section 4.2).
- 3. We searched for coordinated variability across our rapidly varying C IV BAL troughs and find that the velocities over which the variability is coordinated range from ≈290 km s⁻¹ to ≈7250 km s⁻¹ within the troughs. More than half of our troughs show coordinated variations across velocities >1000 km s⁻¹ (see Section 4.3.1). This result is consistent with much of the observed variability being driven by changes in the ionization state of the outflow gas (e.g., Filiz Ak et al. 2013; Grier et al. 2015), which naturally explains coordinated variability across a range of velocities. However, many of our troughs show much smaller ranges of coordinated variability, suggesting that cloud-crossing may be responsible for the variability in other
- 4. We see evidence for coordinated variability between C IV troughs in quasars hosting more than one C IV BAL (see Section 4.3.2). This observation again indicates that the variability cannot be explained solely by a cloud-crossing scenario, as coordinated variability at such a large spread of velocities is difficult to achieve in the context of cloud-crossing models.
- 5. We investigate the presence of other BAL species such as Si IV, Al III, and P V in our sample and find that many of our C IV BALs are saturated; in these cases, cloud-crossing scenarios and/or inhomogeneous partial covering are

- required to explain our observed rapid variability (see Section 4.3.3).
- 6. In many cases, we see variability consistent with models of ionization-state changes within the outflow; we thus adopt a simple model and employ the model to constrain various properties of the outflow in an example object (see Section 4.4). We find outflow density lower limits in agreement with those reported in previous work.

Previous sample-based studies of BAL variability have found significant variability on all timescales explored; we similarly find significant BAL variability down to timescales of less than a day in the quasar rest frame. Our results show that future observational studies of BAL variability on longer timescales need to consider the likely possibility that the BALs have experienced significant variations, perhaps in many directions, within the time span between observations. In addition, models describing BAL formation and variability need to explain short-timescale variability in order to be viable, as such rapid variability is not a rare, extreme phenomenon, but appears to be common among quasars.

Our study is the first to intensively examine short BAL variability timescales (down to less than a day in the quasar rest frame) for many different quasars. Future time-domain spectroscopic studies of quasars will be extremely useful, expanding the sample of quasars searched and placing better constraints on the frequency of such variability. There are multiple upcoming industrial-scale spectroscopic programs that will provide data optimal for such efforts. The SDSS-V Black Hole Mapper program (e.g., Kollmeier et al. 2017) will observe several quasar fields at a high cadence similar to the SDSS-RM, allowing us to explore hundreds of additional BAL quasars and largely expand our sample. Additionally, telescopes such as the 4-Metre Multi-Object Spectroscopic Telescope (4MOST; de Jong et al. 2014) are well-suited for high-cadence spectroscopic studies of quasars, which naturally produce data suitable for short-timescale BAL variability studies. These upcoming programs will be crucial in uncovering the drivers behind this variability and the implications for models of quasar outflows.

Z.S.H., C.J.G., W.N.B., D.P.S., and J.R.T. acknowledge support from NSF grant AST-1517113. W.N.B. and M.V. acknowledge support from NSF grant AST-1516784. P.B.H. acknowledges support from the Natural Sciences and Engineering Research Council of Canada (NSERC), funding reference number 2017-05983. Y.S. acknowledges support from an Alfred P. Sloan Research Fellowship and NSF grant AST-1715579.

Funding for the Sloan Digital Sky Survey IV has been provided by the Alfred P. Sloan Foundation, the U.S. Department of Energy Office of Science, and the Participating Institutions. SDSS-IV acknowledges support and resources from the Center for High-Performance Computing at the University of Utah. The SDSS website is www.sdss.org.

SDSS-IV is managed by the Astrophysical Research Consortium for the Participating Institutions of the SDSS Collaboration, including the Brazilian Participation Group, the Carnegie Institution for Science, Carnegie Mellon University, the Chilean Participation Group, the French Participation Group, Harvard-Smithsonian Center for Astrophysics, Instituto de Astrofísica de Canarias, The Johns Hopkins University, Kavli Institute for the Physics and Mathematics of the Universe

(IPMU) / University of Tokyo, Lawrence Berkeley National Laboratory, Leibniz Institut für Astrophysik Potsdam (AIP), Max-Planck-Institut für Astronomie (MPIA Heidelberg), Max-Planck-Institut für Astrophysik (MPA Garching), Max-Planck-Institut für Extraterrestrische Physik (MPE), National Astronomical Observatory of China, New Mexico State University, New York University, University of Notre Dame, Observatário Nacional/MCTI, The Ohio State University, Pennsylvania State University, Shanghai Astronomical Observatory, United Kingdom Participation Group, Universidad Nacional Autónoma de México, University of Arizona, University of Colorado Boulder, University of Oxford, University of Portsmouth, University of Utah, University of Virginia, University of Washington, University of Wisconsin, Vanderbilt University, and Yale University.

Appendix A Notes on Individual Objects

We here provide additional information and notes on the individual sources in our quasar sample.

A.1. RM 039 (SDSS J141607.12+531904.8)

RM 039 hosts an extremely broad, deep C IV BAL, and it also contains deep Si IV and Al III BALs, placing it into the C IV_{SA} category. This object has a P V BAL at corresponding velocities, indicating that the C IV BAL is highly saturated.

A.2. RM 073 (SDSS J141741.72+530519.0)

RM 073 contains two C IV BALs, neither of which is identified to be significantly variable on short timescales. There is no evidence for corresponding Si IV or Al III BALs or mini-BALs.

A.3. RM 116 (SDSS J141432.46+523154.5)

RM 116 formally has two distinct C IV BALs identified; however, visual inspection of the mean spectrum suggests that these two BALs may belong to the same absorption system. A Si IV absorption feature also exists, as do a few accompanying narrow Al III troughs in the region.

A.4. RM 128 (SDSS J141103.17+531551.3)

RM 128 has two BALs, both identified as rapidly varying but on different dates. In all four epochs exhibiting short-timescale variability, the other BAL also experiences an EW shift in the same direction, but at a lower significance. We interpret this as tentative evidence for coordinated variability, although the low significance of the secondary BAL variability prohibits a definite conclusion. The higher-velocity BAL in RM 128 (BAL[A]) also has a corresponding Si IV BAL as well as slight evidence for shallow Al III absorption at the same velocities. The lower-velocity BAL[B] does not appear to have any accompanying Si IV or Al III absorption.

A.5. RM 155 (SDSS J141123.68+532845.7)

Our spectra for RM 155 do not have complete coverage of the Si IV region; however, we see evidence for the beginning of a Si IV trough at velocities corresponding to those of the very deep C IV BAL, as well as a strong Al III absorption feature. Thus, this is a C IV $_{\rm SA}$ quasar.

A.6. RM 195 (SDSS J141935.58+525710.7)

RM 195 hosts two formal C IV BALs; however, the BAL at higher outflow velocities was excluded from our sample due to the presence of sky line contamination (see Section 3.1). There exists evidence for an Si IV feature accompanying this higher-velocity trough; however, the BAL that is included in our study shows no accompanying Si IV or Al III absorption.

A.7. RM 217 (SDSS J141000.68+532156.1)

This quasar has two identified C IV BALs, but only one is identified as rapidly varying. The high-velocity BAL[A] shows less significant variability—in two epoch pairs, however, the less significant variability is in the same direction as the significant variability. In one epoch pair, the EW of BAL[A] changes in the opposite direction, and it has disappeared completely in the last epoch pair. This quasar is one of two that harbor a high-velocity BAL (BAL[A]) that disappears during the campaign. Additionally, this quasar has Si IV BALs present at velocities corresponding to both C IV BALs, although no Al III absorption is visible.

A.8. RM 257 (SDSS J140931.90+532302.2)

RM 257 has two BALs, both identified as rapidly varying BAL[A] only has two epoch pairs identified as rapidly varying (MJDs 57510–57518 and 57518–57544). BAL[B] is also significantly variable in the same direction during these epoch pairs. In the additional three epoch pairs where BAL[B] is identified as rapidly variable, BAL[A] also varies in the same direction, but the variability is significant at less than 4σ . Thus, we again find tentative evidence for coordinated variability. RM 257 BAL[A] has accompanying Si IV and Al III troughs. The PV region corresponding to these velocities is cut off at the blue end of the wavelength region, but the spectrum does appear to have PV absorption.

A.9. RM 284 (SDSS J141927.35+533727.7)

RM 284 shows broad C IV absorption within our velocity search range—however, this quasar also has a very highvelocity C IV trough (not studied in this work) extending from approximately 35,000 to 59,000 km s⁻¹ with a maximum depth of approximately 50% of the continuum flux. The absorption EW of the very high-velocity trough has generally decreased from 2014 to 2017, but the maximum depth has not. We see the red edge of an accompanying very high-velocity N V absorption trough at the extreme blue edge of the SDSS-RM spectrum, but we lack coverage of the PV region at these velocities. The strength of any Si IV absorption in BAL[A] in this quasar is impossible to determine, due to confusion with the very high-velocity C IV trough, so we assign the C IV_{NO} designation to this target in order to indicate this uncertainty. There does not appear to be substantial Al III absorption, although the region blueward of Al III has considerable blended Fe emission, making it difficult to interpret the spectrum.

A.10. RM 339 (SDSS J142014.84+533609.0)

RM 339 contains BAL troughs in both Si IV and Al III at velocities similar to those of the C IV trough. Thus, this is a C IV $_{\rm SA}$ trough.

A.11. RM 357 (SDSS J141955.27+522741.1)

RM 357 has two C IV BAL troughs. BAL[A], the higher-velocity BAL, displays rapid variability on two separate occasions. On both of those occasions, BAL[B] also exhibits rapid variability in the same direction. BAL[B] shows rapid variability in five additional epoch pairs as well, but in two of these pairs, BAL[A] has disappeared entirely. In the epoch pairs where BAL[A] remains present, it varies in the same direction as BAL[B], but at a lower significance. Thus, we yet again see tentative evidence for coordinated variability. RM 357 BAL[B] has accompanying Si IV absorption, but no signs of Al III features. The P V region is not covered by our spectra for this quasar.

A.12. RM 361 (SDSS J142100.22+524342.3)

RM 361 has a single, deep BAL trough. The Si IV region is not covered by our spectra, so we assign this BAL to the C IV $_{
m N0}$ category. There is not strong evidence for Al III absorption.

A.13. RM 408 (SDSS J141409.85+520137.2)

RM 408 has visible narrow Si IV and Al III absorption at velocities corresponding to the C IV BAL[A]; however, both of these features are too narrow to meet our formal BAL definition, so we assign this BAL to the C IV $_{00}$ category. We do not have coverage of the P V region in this object.

A.14. RM 508 (SDSS J142129.40+522752.0)

This quasar exhibits C IV absorption with no accompanying Si IV, Al III, or P V features. Additional C IV absorption is visible, at lower velocities, that is both slightly too shallow and narrow to meet the formal BAL definition. The C IV BAL[A] in this target varies significantly on short timescales, sometimes with exceptionally high significance (i.e., greater than $20\sigma_{\Delta \rm EW}$), making this quasar especially noteworthy. There also may be a weak, broad, very high-velocity C IV absorption feature at rest frame 1350 Å.

A.15. RM 509 (SDSS J142233.74+525219.8)

RM 509 has two C IV BALs, but only the lower-velocity BAL[B] is rapidly variable. This variability only occurs in a single pair of epochs. Between this rapidly varying pair of epochs, BAL[A] varies in the same direction but at lower significance. The higher-velocity BAL[A] has an accompanying Si IV trough, but no Al III feature; the lower-velocity BAL [B] shows no BALs or mini-BALs of either species. There is no evidence for a P V BAL in this target.

A.16. RM 564 (SDSS J142306.05+531529.0)

This source has a high-velocity C IV BAL with accompanying Si IV absorption, but no Al III feature. We also see a significant feature near 1320 Å in the Si IV region that must be an extremely high-velocity C IV trough.

A.17. RM 565 (SDSS J140634.14+525407.8)

The spectra for RM 565 barely clear our SN threshold; it is thus difficult to identify different species throughout the spectra. However, we identify two BALs in this quasar. The velocities covered by BAL[A] are not fully covered by the spectra in the Si IV region, so we are unsure whether

Si IV is present at these velocities. Al III does not appear to be present in the spectra. The lower-velocity BAL[B] appears to have accompanying Si IV absorption but no Al III absorption.

A.18. RM 613 (SDSS J141007.73+541203.4)

RM 613 has one C IV BAL that meets the formal BAL definition, although there is an additional lower-velocity mini-BAL. Si IV absorption is likely present at velocities corresponding to the BAL, but, at <10% of the continuum flux, it does not formally meet the definition of a BAL. There is no evidence for accompanying Al III absorption. This quasar was investigated by Grier et al. (2015), hereafter G15, who reported the first detection of significant BAL variability on timescales shorter than five days in the quasar rest frame. Their investigation revealed four different pairs of spectra separated by less than five rest-frame days that exhibited $>4\sigma_{\Delta \rm EW}$ BAL variability. We find qualitatively similar results in our study (i.e., the BAL varies on short timescales in several epoch pairs); however, we identify fewer (and different) pairs of epochs as significantly variable.

The identified variable epoch pairs from G15 are MJDs 56697-56715 (Pair 1), MJDs 56751-56755 (Pair 2), MJDs 56768-56772 (Pair 3), and MJDs 56783-56795 (Pair 4). Pair 2 was also identified in our study as significantly variable. Pairs 1 and 4 were not identified in our study due to the implementation of the G criterion, and Pair 3 was not identified due to the re-binning of the spectra causing the ΔEW value to fall just below our 4σ significance threshold. In addition, we identify two additional significantly variable epoch pairs that were not noted by G15; prior to the spectral binning, these epoch pairs were also just below the 4σ significance cutoff. We do not believe the epochs identified by G15 are in error; in fact, we find it likely that all of these epoch pairs show real BAL variability. We again stress our goal of assembling a clean, conservative collection of significant BAL variations in this study, and our strict significance criteria is likely to eliminate some epoch pairs that exhibit true variability.

A.19. RM 631 (SDSS J140554.87+530323.5)

This quasar has a C IV BAL accompanied by Si IV absorption. Additionally, a Al III absorption feature exists, but it does not drop down below a normalized flux density of 0.9. Thus, this is a C IV $_{\rm SO}$ BAL. However, strong evidence for Al III exists, and evidence for P V is apparent as well.

A.20. RM 717 (SDSS J141648.26+542900.9)

RM 717 exhibits a broad C IV BAL with multiple components; we see a similar structure in the accompanying Si IV BAL at corresponding velocities. Hints of possible similarly structured Al III absorption are visible, but the flux does not drop below 0.9 at any point.

A.21. RM 722 (SDSS J142419.18+531750.6)

This object displays a single C IV BAL with no accompanying broad Si IV or Al III absorption, though there is narrow Si IV absorption superimposed on the Si IV emission line.

A.22. RM 729 (SDSS J142404.67+532949.3)

RM 729 contains a fairly deep C IV BAL trough with accompanying Si IV absorption and traces of accompanying

Al III absorption. The Al III absorption is not quite deep enough to be considered a formal BAL or mini-BAL. There is potential evidence for a PV BAL feature, though the low SN in the PV region makes this uncertain. RM 729 also has a second formal C IV BAL present in its spectrum at higher velocity; however, it was excluded from our study due to contamination by bad pixels (see Section 3.1).

A.23. RM 730 (SDSS 142225.03+535901.7)

RM 730 possesses two C IV BALs that are very close together (see Figure 3), though they are detected as two distinct BALs separated by about 500 km s⁻¹ (see their $v_{\rm min}$ and $v_{\rm max}$ measurements in Table 3). The higher-velocity BAL [A] shows significant short-term variability in two pairs of epochs; BAL[B] in this object does not vary significantly over these time periods. BAL[A] shows coordinated variability on velocity scales of 750 and 1250 km s⁻¹ (only about 5% and 9% of the entire trough width) during the two identified epoch pairs. There is a Si IV BAL present at velocities corresponding to BAL[A], and traces of Al III absorption, but the Al III features are too shallow to be considered BALs; we thus place this trough into the C IV_{S0} category. There is no evidence for Si IV, Al III, or P V BALs or mini-BALs at velocities corresponding to the lower-velocity BAL[B].

A.24. RM 743 (SDSS J142405.10+533206.3)

RM 743 has strong C IV, Si IV, and Al III BAL features present. In addition, Al II λ 1670 (and probably Mg II) absorption also appears in this quasar.

This quasar shows no Si IV or Al III absorption.

This source has a single C IV BAL, accompanied by Si IV absorption. There are potential P V BALs at corresponding velocities, although the low SN of the region makes this a tentative interpretation.

A.27. RM 786 (SDSS J141421.53+522940.1)

RM 786 has a very shallow high-velocity BAL[A] that varies rapidly for one epoch pair. For the same epoch pair, the low-velocity, deeper BAL[B] varies in the same direction, suggesting coordinated variability between the two. BAL[B] varies significantly in many more epochs, however—sometimes BAL[A] varies in the same direction, but for two epoch pairs, the troughs vary in opposite directions. Again, we note that the BAL[A] is varying at low significance in these cases, so the disagreement is tentative rather than conclusive.

Appendix B Derivation of Physical Constraint Equations

We below provide details on the model and calculations discussed in Section 4.4.

B.1. Ionization Variability Model

In a simple ionization-variability scenario, a step-function change in ionizing flux by some factor A alters the ionization balance in the absorber, resulting in a change in the observed

optical depth of a given tracer ion by a factor B on a density-dependent equilibration timescale. If the electron density in the absorber is constant over its velocity range, then the equilibration timescale and the factor B will be constant with velocity as well. ¹³

We can test for this predicted optical-depth change by a constant factor by assuming a uniform partial-covering scenario (e.g., de Kool et al. 2002). We perform this test for the two epochs in which RM 508 shows the greatest change in its absorption depth (MJDs 57901 and 57918). For these two epochs, hereafter denoted 1 and 2, we take the normalized flux profile in the $2900 \, \mathrm{km \, s^{-1}}$ wide trough and bin by three pixels to reduce correlations between pixels. We assume a value of the covering factor C and calculate

$$\tau_1(\lambda) = -\ln[(F_1(\lambda) + 1 - C)/C]$$

$$\tau_2(\lambda) = -\ln[(F_2(\lambda) + 1 - C)/C]$$

and the ratio $B(\lambda) = \tau_1(\lambda)/\tau_2(\lambda)$, as well as the accompanying uncertainties (we are approximating the C IV doublet as a singlet because the trough is broader than the doublet separation). We then find the weighted average \bar{B} over the entire trough. We simultaneously fit the trough profiles with the above partial-covering model with those values of C and \bar{B} and a 14-point optical depth profile (one for each velocity), determined using both F_1 and F_2 at each velocity. Mathematically, we fit C, \bar{B} , and 14 values of $\tau_{1, \text{ model}}$ (one at each pixel), where

$$\tau_{1,\text{model}} = -(\ln[(F_1(\lambda) + 1 - C)/C]$$

+\bar{B}\ln[(F_2(\lambda) + 1 - C)/C])/2
and \tau_{2,\text{model}} = \tau_{1,\text{model}}/\bar{B}.

We repeat this exercise for all possible values of $C \le 1$. We find a minimum $\chi^2 = 22.3$ for 12 degrees of freedom for C = 1, which is a marginally acceptable model ($p = 3.48 \times 10^{-2}$, 1.82σ). The relatively large minimum χ^2 may indicate that the adopted model is an oversimplification, or it may arise from the use of only two epochs of data to fit the optical-depth profile. Our results indicate that the observed variability is consistent with a model of an absorber that fully covers the continuum source, is optically thin in C IV (with a maximum optical depth $\tau_{\rm max} = 0.847 \pm 0.024$), has constant electron density over its velocity range, and responds to a variable ionizing flux by a drop in optical depth of a factor of $\bar{B} = 2.04 \pm 0.07$ in 4.03 rest-frame days.

B.2. Density Constraint

Following Grier et al. (2015), we further use the observed changes in EW and the timescale of these changes to measure a lower limit on the density of the outflow material. For ionization state i of some element that begins in photoionization equilibrium, the density of species n_i can be modeled as varying with a characteristic timescale t_i^* as

$$n_i(t) = n_i(0)\exp(t/t_i^*) \tag{6}$$

(Arav et al. 2012; Rogerson et al. 2015). Assuming the outflow is optically thin, number density is linearly proportional to

 $[\]overline{^{13}}$ A step function is just one member of a family of ionizing-flux light curves that will create an optical-depth change of a factor B between two given epochs. We are not concerned here with reconstructing the true ionizing flux light curve, merely with testing whether the resulting optical depth change is constant with velocity.

column density. Thus, for the case of two relevant quasar observations, $n_i(t)/n_i(0) = \mathrm{EW}_2/\mathrm{EW}_1$, and $t = \Delta t_{\mathrm{rest}}$. Equation (6) can therefore be rewritten and solved for the characteristic timescale t_i^* , giving

$$t_i^* = \Delta t_{\text{rest}} \log(\text{EW}_2/\text{EW}_1)^{-1}. \tag{7}$$

Using the ionization rate per ion of state $i(I_i)$, the ion's recombination coefficient to ionization state i-1 (α_{i-1}), and the fractional change in I_i (f_i , for which $f_i = I_i(t)/I_i(0) - 1$ and $-1 < f_i < +\infty$), the characteristic timescale t_i^* can also be calculated as

$$t_i^* = [-f_i(I_i - n_e \alpha_{i-1})]^{-1}$$
(8)

assuming photoionization and recombination are the only processes relevant to ionization state change (i.e., collisional ionization is ignored). A negative t_i^* implies n_i decreasing with time.

For an outflow sufficiently separated from the quasar, recombination dominates photoionization $(n_e\alpha_{i-1} \gg I_i)$. Consider the scenario in which ionizing flux vanishes, implying $f_i = -1$ (e.g., Capellupo et al. 2013). For this limiting case, t_i^* is the recombination time of the ion, and Equation (8) reduces to $t_i^* = -1/n_e\alpha_{i-1}$. Holding firm our previous assumption of optical thinness, this result can be combined with Equation (7) to derive the lower density limit

$$n_e > \log(EW_1/EW_2)/\alpha_{i-1}\Delta t_{rest}$$
 (9)

that is Equation (4), used to constrain outflow density in Section 4.4

B.3. Radial Distance Constraint

For an optically thin cloud containing some element in ionization state i at radial distance r from a quasar with luminosity L_{ν} , the ionization rate per ion in state i is calculated as

$$I_i = \int_{\nu_i}^{\infty} \frac{(L_{\nu}/h\nu)\sigma_{\nu}}{4\pi r^2} d\nu \tag{10}$$

for which σ_{ν} is the ionization cross section for photons of energy $h\nu$ and ν_i is the ionization energy of ionization species (i-1).

In the derivation of our density constraint (see Appendix B.2), we assume that the outflow is sufficiently separated from the quasar such that recombination (with recombination coefficient α_{i-1}) dominates photoionization ($I_i \ll n_e \alpha_{i-1}$). As radial distance from the quasar decreases, ionizing flux increases and photoionization comes to instead dominate recombination ($I_i \gg n_e \alpha_{i-1}$). Between photoionization-dominated distances and recombination-dominated distances exists an equilibrium distance (r_{equal}) for which the rate of photoionization and the rate of recombination are equivalent ($I_i = n_e \alpha_{i-1}$). Due to the aforementioned assumptions of our density constraint derivation, this constraint is only valid at distances larger than the equilibrium distance ($r > r_{\text{equal}}$). From these arguments, we substitute $I_i = n_e \alpha_{i-1}$ and $r > r_{\text{equal}}$ into Equation (10), obtaining the lower radial distance limit

$$r > r_{\text{equal}} = \sqrt{\int_{\nu_i}^{\infty} \frac{(L_{\nu}/h\nu)\sigma_{\nu}}{4\pi n_e \alpha_{i-1}} d\nu}$$
 (11)

that is Equation (5), used to constrain the radial distance of outflows in Section 4.4.

ORCID iDs

```
Z. S. Hemler https://orcid.org/0000-0002-0799-0225
C. J. Grier https://orcid.org/0000-0001-9920-6057
W. N. Brandt https://orcid.org/0000-0002-0167-2453
P. B. Hall https://orcid.org/0000-0002-1763-5825
Keith Horne https://orcid.org/0000-0003-1728-0304
Yue Shen https://orcid.org/0000-0003-1659-7035
J. R. Trump https://orcid.org/0000-0002-1410-0470
Dmitry Bizyaev https://orcid.org/0000-0002-3601-133X
Kaike Pan https://orcid.org/0000-0002-2835-2556
```

References

```
Ahn, C. P., Alexandroff, R., Allende Prieto, C., et al. 2014, ApJS, 211, 17
Arav, N., Borguet, B., Chamberlain, C., Edmonds, D., & Danforth, C. 2013,
   MNRAS, 436, 3286
Arav, N., Edmonds, D., Borguet, B., et al. 2012, A&A, 544, A33
Arav, N., Kaastra, J., Kriss, G. A., et al. 2005, ApJ, 620, 665
Arav, N., Liu, G., Xu, X., et al. 2018, ApJ, 857, 60
Arav, N., Moe, M., Costantini, E., et al. 2008, ApJ, 681, 954
Barlow, T. A. 1993, PhD thesis, California Univ.
Baskin, A., Laor, A., & Stern, J. 2014, MNRAS, 445, 3025
Blanton, M. R., Bershady, M. A., Abolfathi, B., et al. 2017, AJ, 154, 28
Borguet, B. C. J., Arav, N., Edmonds, D., Chamberlain, C., & Benn, C. 2013,
     pJ, 762, 49
Capellupo, D. M., Hamann, F., Herbst, H., et al. 2017, MNRAS, 469, 323
Capellupo, D. M., Hamann, F., Shields, J. C., Halpern, J. P., & Barlow, T. A.
   2013, MNRAS, 429, 1872
Capellupo, D. M., Hamann, F., Shields, J. C., Rodríguez Hidalgo, P., &
   Barlow, T. A. 2011, MNRAS, 413, 908
Capellupo, D. M., Hamann, F., Shields, J. C., Rodríguez Hidalgo, P., &
Barlow, T. A. 2012, MNRAS, 422, 3249
Cardelli, J. A., Clayton, G. C., & Mathis, J. S. 1989, ApJ, 345, 245
Dawson, K. S., Kneib, J.-P., Percival, W. J., et al. 2016, AJ, 151, 44
Dawson, K. S., Schlegel, D. J., Ahn, C. P., et al. 2013, AJ, 145, 10
De Cicco, D., Brandt, W. N., Grier, C. J., et al. 2018, A&A, 616, A114
de Jong, R. S., Barden, S., Bellido-Tirado, O., et al. 2014, Proc. SPIE, 9147,
de Kool, M., Korista, K. T., & Arav, N. 2002, ApJ, 580, 54
Dere, K. P., Landi, E., Mason, H. E., Monsignori Fossi, B. C., & Young, P. R.
             AS, 125, 149
Di Matteo, T., Springel, V., & Hernquist, L. 2005, Natur, 433, 604
Dunn, J. P., Bautista, M., Arav, N., et al. 2010, ApJ, 709, 611
Eisenstein, D. J., Weinberg, D. H., Agol, E., et al. 2011, AJ, 142, 72
Filiz, Ak, N., Brandt, W. N., Hall, P. B., et al. 2012, ApJ, 757, 114
Filiz, Ak, N., Brandt, W. N., Hall, P. B., et al. 2013, ApJ, 777, 168
Filiz, Ak, N., Brandt, W. N., Hall, P. B., et al. 2014, ApJ, 791, 88
Gehrels, N. 1986, ApJ, 303, 336
Gibson, R. R., Brandt, W. N., Gallagher, S. C., Hewett, P. C., &
   Schneider, D. P. 2010, ApJ, 713, 220
Gibson, R. R., Brandt, W. N., Gallagher, S. C., & Schneider, D. P. 2009a, ApJ,
Gibson, R. R., Brandt, W. N., & Schneider, D. P. 2008, ApJ, 685, 773
Gibson, R. R., Jiang, L., Brandt, W. N., et al. 2009b, ApJ, 692, 758 Grier, C. J., Brandt, W. N., Hall, P. B., et al. 2016, ApJ, 824, 130
Grier, C. J., Hall, P. B., Brandt, W. N., et al. 2015, ApJ, 806, 111
Gunn, J. E., Siegmund, W. A., Mannery, E. J., et al. 2006, AJ, 131, 2332
Haggard, D., Arraki, K. S., Green, P. J., Aldcroft, T., & Anderson, S. F. 2012,
   in ASP Conf. Ser. 460, AGN Winds in Charleston, ed. G. Chartas,
   F. Hamann, & K. M. Leighly (San Francisco, CA: ASP), 98
Hall, P. B., Anosov, K., White, R. L., et al. 2011, MNRAS, 411, 2653
Hall, P. B., Sadavoy, S. I., Hutsemekers, D., Everett, J. E., & Rafiee, A. 2007,
   ApJ, 665, 174
Hamann, F. W., Netzer, H., & Shields, J. C. 2000, ApJ, 536, 101
He, Z.-C., Bian, W.-H., Ge, X., & Jiang, X.-L. 2015, MNRAS, 454, 3962
He, Z., Wang, T., Zhou, H., et al. 2017, ApJS, 229, 22
Higginbottom, N., Knigge, C., Long, K. S., Sim, S. A., & Matthews, J. H.
   2013, MNRAS, 436, 1390
```

Higginbottom, N., Proga, D., Knigge, C., et al. 2014, ApJ, 789, 19

```
King, A., & Pounds, K. 2015, ARA&A, 53, 115
Kollmeier, J. A., Zasowski, G., Rix, H.-W., et al. 2017, arXiv:1711.03234
Krolik, J. H. 1999, Active Galactic Nuclei: from the Central Black Hole to the
  Galactic Environment (Princeton, NJ: Princeton Univ. Press)
Landi, E., Young, P. R., Dere, K. P., Del Zanna, G., & Mason, H. E. 2013,
Lundgren, B. F., Wilhite, B. C., Brunner, R. J., et al. 2007, ApJ, 656, 73
Marshall, H. L., Carone, T. E., Peterson, B. M., et al. 1997, ApJ, 479, 222
Misawa, T., Kawabata, K. S., Eracleous, M., Charlton, J. C., & Kashikawa, N.
   2010, ApJ, 719, 1890
Moll, R., Schindler, S., Domainko, W., et al. 2007, A&A, 463, 513
Murray, N., Chiang, J., Grossman, S. A., & Voit, G. M. 1995, ApJ, 451, 498
Pâris, I., Petitjean, P., Aubourg, É., et al. 2018, A&A, 613, A51
Park, D., Woo, J.-H., Denney, K. D., & Shin, J. 2013, ApJ, 770, 87
Pei, Y. C. 1992, ApJ, 395, 130
Proga, D. 2000, ApJ, 538, 684
Proga, D., Rodriguez-Hidalgo, P., & Hamann, F. 2012, in ASP Conf. Ser. 460,
   AGN Winds in Charleston, ed. G. Chartas, F. Hamann, & K. M. Leighly
   (San Francisco, CA: ASP), 171
Richards, G. T., Strauss, M. A., Fan, X., et al. 2006, AJ, 131, 2766
Rogerson, J. A., Hall, P. B., Ahmed, N. S., et al. 2018, ApJ, 862, 22
```

```
Rogerson, J. A., Hall, P. B., Rodríguez Hidalgo, P., et al. 2016, MNRAS,
  457, 405
Sabra, B. M., & Hamann, F. 2005, arXiv:astro-ph/0310668
Schlafly, E. F., & Finkbeiner, D. P. 2011, ApJ, 737, 103
Shen, Y., Brandt, W. N., Dawson, K. S., et al. 2015, ApJS, 216, 4
Shen, Y., Hall, P. B., Horne, K., et al. 2018, arXiv:1810.01447
Shen, Y., Horne, K., Grier, C. J., et al. 2016, ApJ, 818, 30
Smee, S. A., Gunn, J. E., Uomoto, A., et al. 2013, AJ, 146, 32
van der Marel, R. P., & Franx, M. 1993, ApJ, 407, 525
Vanden Berk, D. E., Richards, G. T., Bauer, A., et al. 2001, AJ, 122, 549
Vivek, M., Srianand, R., & Gupta, N. 2016, MNRAS, 455, 136
Vivek, M., Srianand, R., Mahabal, A., & Kuriakose, V. C. 2012, MNRAS,
  421, L107
Vivek, M., Srianand, R., Petitjean, P., et al. 2014, MNRAS, 440, 799
Wang, T., Yang, C., Wang, H., & Ferland, G. 2015, ApJ, 814, 150
Welling, C. A., Miller, B. P., Brandt, W. N., Capellupo, D. M., &
  Gibson, R. R. 2014, MNRAS, 440, 2474
Weymann, R. J., Morris, S. L., Foltz, C. B., & Hewett, P. C. 1991, ApJ, 373, 23
White, R. L., Becker, R. H., Helfand, D. J., & Gregg, M. D. 1997, ApJ,
Xu, X., Arav, N., Miller, T., & Benn, C. 2018, ApJ, 858, 39
```